Coherent Elastic Neutrino-Nucleus Scattering at the Japan Proton Accelerator Research Complex

J.I. Collar,[1,2,3,*] Ivan Esteban,[4,5,†] J.J. Gomez-Cadenas,[2,3] M. C. Gonzalez–Garcia,[6,7,8,‡] L.-C. Ji,[2] L. Larizgoitia,[2] C.M. Lewis,[1,2] F. Monrabal,[2,3] João Paulo Pinheiro.,[9,10,§] A. Simón,[2,11] and S.G. Yoon[1]

[1] *Enrico Fermi Institute, Kavli Institute for Cosmological Physics, and Department of Physics University of Chicago, Chicago, Illinois 60637, USA*

[2] *Donostia International Physics Center, Paseo Manuel Lardizabal 4, 20018, Donostia-San Sebastián, Spain*

[3] *Ikerbasque, Basque Foundation for Science, Plaza Euskadi 5, 48013, Bilbao, Spain*

[4] *Department of Physics, University of the Basque Country UPV/EHU, PO Box 644, 48080 Bilbao, Spain*

[5] *EHU Quantum Center, University of the Basque Country UPV/EHU, PO Box 644, 48080 Bilbao, Spain*

[6] *Departament de Fisica Quantica i Astrofisica and Institut de Ciencies del Cosmos, Universitat de Barcelona, Diagonal 647, E-08028 Barcelona, Spain*

[7] *Institució Catalana de Recerca i Estudis Avancats (ICREA) Pg. Lluis Companys 23, 08010 Barcelona, Spain.*

[8] *C.N. Yang Institute for Theoretical Physics, Stony Brook University, Stony Brook NY11794-3849, USA*

[9] *State Key Laboratory of Dark Matter Physics, Tsung-Dao Lee Institute & School of Physics and Astronomy, Shanghai Jiao Tong University, Shanghai 200240, China*

[10] *Key Laboratory for Particle Astrophysics and Cosmology (MOE) & Shanghai Key Laboratory for Particle Physics and Cosmology, Shanghai Jiao Tong University, Shanghai 200240, China*

[11] *Instituto de Física Corpuscular, CSIC & Universitat de València, Calle Catedrático José Beltrán 2, 46980, Paterna, Spain*

(Dated: May 15, 2026)

The Japan Proton Accelerator Research Complex (J-PARC) currently delivers a 1 MW, 3 GeV proton beam to the Materials and Life Science Experimental Facility (MLF). Power is expected to increase to 1.3 MW, driven by the needs of Hyper-Kamiokande. As a result, the MLF presently provides the highest neutron yield of any spallation source, while potentially holding the best current and foreseeable conditions for Coherent Elastic Neutrino-Nucleus Scattering (CEνNS) experimentation. We explore this potential, using as examples detector technologies presently funded for construction and under development. We quantify their sensitivity to a rich variety of particle physics scenarios, finding that very-high-statistics CEνNS measurements with significant sensitivity to relevant scenarios are feasible at this facility within the next few years.

arXiv:2512.19788v4 [hep-ph] 14 May 2026

I. INTRODUCTION

The most probable interaction mechanism for low-energy neutrinos is their elastic scattering off atomic nuclei, mediated by the neutral electroweak current. For neutrino energies below few tens of MeV the momentum exchange with the recoiling nucleus is sufficiently low that the interaction must be regarded as involving the nucleus as a whole. This coherent phenomenon leads to a large enhancement to the elastic scattering cross section of this process: it becomes proportional to the square of the number of nucleons, although the numerical value of the weak mixing angle makes the neutron contribution dominate [1]. This process (Coherent Elastic Neutrino-Nucleus Scattering, CEνNS) provides a new path to explore both neutrino properties and nuclear structure. It also leads to a drastic reduction in neutrino detector mass when compared to all other known means of neutrino interaction.

The experimental challenge resides in the fact that this process produces a single observable, a recoiling nucleus carrying a modest kinetic energy in the few-keV to sub-keV range, as is also the case in neutron elastic scattering and for the expected interactions from certain Dark Matter candidates. For most targets only a small fraction of this energy is converted into a readily detectable form, e.g., ionization or scintillation: this energy-dependent conversion efficiency is commonly referred to as a "quenching factor" (QF). Its characterization is necessary for the interpretation of these faint neutrino signals. As a result, QF measurements presently constitute an active area of research involving numerous neutrino and Dark Matter detector materials.

Altogether this resulted in the four decades spanning

* collar@uchicago.edu
† ivan.esteban@ehu.eus
‡ concha.gonzalez-garcia@stonybrook.edu
§ joaopaulo.pinheiro@fqa.ub.edu

between the theoretical description of CEνNS [1] and its experimental observation [2, 3] being consumed by a search for a viable combination of neutrino source and detector. The first was provided by the Spallation Neutron Source (SNS) at Oak Ridge National Laboratory, the highest-power facility of this type at the time [4, 5]. The second, by sodium-doped cesium iodide (CsI[Na]), an inorganic scintillator with ideal characteristics for this measurement [6, 7]. This long interval allowed for the development of a broad variety of CEνNS applications in nuclear and particle physics phenomenology: searches for electromagnetic properties of the neutrino, for non-standard neutrino-quark interactions facilitated by new mediators, studies of weak nuclear charge and nuclear structure, evidence for sterile neutrinos and potential Dark Matter candidates, etc. An abridged list of the numerous publications in this area is provided in Sec. V of this work. The miniaturization that is possible with CEνNS detectors may also lead to eventual technological applications [8].

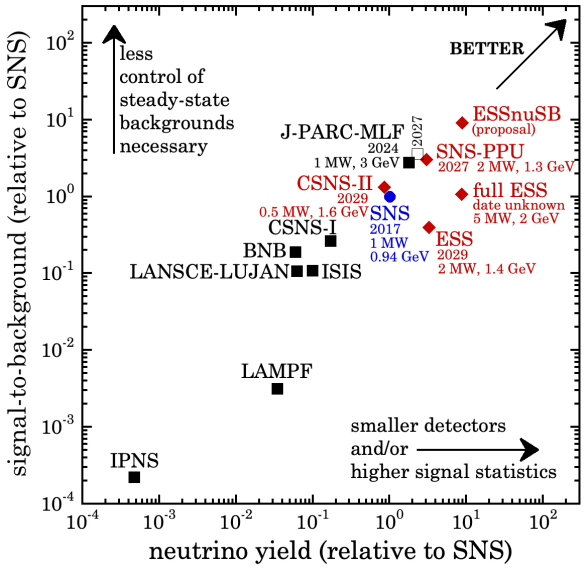

FIG. 1. Comparison between past and present (black squares) and future (red diamonds) spallation sources from the perspective of CEνNS detection, taking as reference the SNS (blue circle) at the time of first observation of this process [2]. A hollow square represents J-PARC MLF following the impending upgrade to 1.3 MW (see text).

In a seminal paper, Drukier and Stodolsky [9] examined the applicability of different neutrino sources to CEνNS experimentation, concluding that spallation sources are the most immediately convenient. While those are mainly dedicated to neutron production, the decay-at-rest (DAR) of positive pions generated during the stopping of energetic protons in the spallation target also results in a high yield of three flavours of neutrinos (ν_μ, $\overline{\nu}_\mu$, ν_e) having well-established spectral and timing characteristics as we discuss below [4, 5]. All are able to participate in the coherent process described above. The pulsed nature of this flux helps reduce the impact of steady-state environmental backgrounds on CEνNS detectors, and the relatively-high neutrino energy (up to the limit where coherence starts to wane) results in easier-to-detect few-keV nuclear recoils. Lower-energy electron antineutrinos from nuclear power reactors provide a significantly higher flux in proximity to their cores, yet without the benefit of a known time of arrival for CEνNS signals. Additionally, these reactor $\overline{\nu}_e$ generate harder-to-detect sub-keV recoils, for which the acquisition of a reliable knowledge of the QF is more of a challenge. To illustrate the difficulties involved, a first measurement of reactor CEνNS [10] is now disputed in [11], with the adopted QF for sub-keV germanium recoils playing a critical role in resolving this tension [12]. This situation will soon be clarified by upcoming results from the upgraded detector in [10], now operating at the Vandellòs-II nuclear power plant, together with a novel precision measurement of the sub-keV QF in this medium. However, in view of it, it seems prudent to regard spallation facilities as the most reliable sources of CEνNS information, at least for the near future. The recent detection of CEνNS from comparatively low-flux solar neutrinos [13–15] is to provide useful contributions [16, 17] albeit limited by expected low statistics, even when the multi-tonne mass of the Dark Matter detectors involved is considered.

Six years ago we described the prospects of the future European Spallation Source (ESS) for CEνNS work [18]. In the interim, significant delays have affected the completion of the ESS. Whereas a design power of 5 MW and proton energy of 2 GeV was originally planned for 2027, the present goal has dwindled to 2 MW and 1.4 GeV in 2029, with additional delays possible given the novelty of its target design. This significantly impacts the immediate relevance of the ESS in this field, while the ESSnuSB expansion proposal [19] maintains great promise (Fig. 1). During this same period, the Japan Proton Accelerator Research Complex (J-PARC) has ramped up the power of its 3 GeV proton beam delivery to the Materials and Life Science Experimental Facility (MLF) to 1 MW, with an increase to 1.3 MW by 2027 being driven by the needs of the Hyper-Kamiokande detector. As a result, the MLF presently provides not only the highest neutron yield of any spallation source [20], but also the best current and foreseeable conditions for CEνNS experimentation.

To illustrate this, Fig. 1 (updated from [21]) provides a balanced comparison between spallation sources in the context of CEνNS. The horizontal axis involves an explicit calculation of neutrino yield that includes the combined effect of proton energy, spallation target material, and beam current [18] instead of just beam power as in, e.g., Refs. [22, 23]. The signal-to-background-ratio figure of merit along the vertical axis acknowledges the ability to assess —and later subtract— steady-state backgrounds during periods of anticoincidence with protons-on-target (POT), folding in the duty cycle of each source and assigning to all a common 10 μs post-POT window for the detection of delayed $\overline{\nu}_\mu$ and ν_e from μ^+ decay

following π^+ DAR [21].

In this work, we analyze the potential of J-PARC MLF for CEνNS studies, using as examples detector technologies presently funded for construction and under development. We nevertheless consider an extrapolation to a future detector mass of order one tonne. We find that for targets relatively straightforward to scale-up (e.g., cesium iodide) this represents a point of diminishing returns, one where the improvement in sensitivity to several parameters of phenomenological interest is no longer limited by this factor (the exposure, as determined by detector mass) but instead is impacted by irreducible uncertainties associated to a realistically-achievable knowledge of QF and neutrino flux.

The structure of this paper is as follows. Sec. II describes the neutrino yield and signal structure expected at J-PARC MLF, listing additional advantages of this facility for CEνNS studies. Sec. III describes the sources of background, both beam-related and environmental (i.e., steady-state) that would affect detector technologies presented in Sec. IV, during their deployment at the MLF. Background simulations derived from this information are used for the calculations of physics reach presented in Sec. V. Our conclusions are presented in Sec. VI.

II. NEUTRINO YIELD AT J-PARC MLF

As described above, in a neutron spallation source neutrinos are mainly produced by the pion DAR $\pi^+ \to \mu^+ \nu_\mu$ followed by the muon DAR $\mu^+ \to e^+ \bar{\nu}_\mu \nu_e$ [24]. The energy distribution is very-well understood: for π^+ two-body decay neutrinos are monochromatic, for μ^+ the SM provides a clean prediction [4, 5, 25]. We provide analytic expressions in Sec. V A. The main uncertainty is the overall normalization, i.e., the number of pions produced per proton hitting the target.

In this respect, an additional significant advantage of J-PARC MLF is the eventual ability of the existing JSNS^2 detectors [26] to measure the local neutrino flux via the $^{12}C(\nu_e, e^-)^{12}N_{g.s.}$ reaction down to a 10% uncertainty level [26]. A dedicated effort as has been proposed at other facilities [27] could reduce this further down to the 2%–5% level. Here, we assume a positive pion production per 3 GeV proton of 0.44 π^+/p at the MLF mercury target, derived from MCNPX simulations [28] (ISABEL/Dresner intranuclear/evaporation models) like those described in Ref. [18]. This is consistent with a recent JSNS^2 first *in situ* measurement of 0.48 ± 0.17 π^+/p [29]. Our adopted pion production translates into a neutrino yield of 3.89×10^{22} ν per flavour per year of continuous operation for 1.3 MW power delivery (the yearly operational schedule of MLF is included in Sec. V). For perspective, this π^+/p production was ~0.078 at the SNS at the time of the first CEνNS observation, a result of its marked dependence on proton energy [18] (Fig. 1).

An additional advantage of J-PARC MLF, compared to the original prospects for the ESS [18], is the pulsed nature of the proton beam: 25 Hz of 0.1 μs-wide double pulses separated by 0.54 μs [24]. As a consequence, ν_μ from π^+ decay, produced simultaneously with protons hitting the target due to the short pion lifetime $\tau_\pi \simeq 0.03\,\mu$s can be well-separated from $\bar{\nu}_e$ and $\bar{\nu}_\mu$ from μ^+, produced after timescales of order the muon lifetime $\tau_\mu \simeq 2\,\mu$s. This significantly boosts physics searches for flavour-dependent effects, that can exploit the time structure of the neutrino signal irrespective of flux normalization uncertainties. We provide explicit expressions and illustrate this further in Sec. V A.

III. BACKGROUND SOURCES AFFECTING A CEνNS SEARCH

Neutrino signals from CEνNS at an spallation source present a characteristic structure in both energy and time [4, 5, 18]. This facilitated the first experimental observation of this process [2, 3]. The time dependence, which closely traces the periodic injection of short proton spills into the spallation target, allows to reduce the impact of the environmental (i.e., steady-state) backgrounds that continuously affect detectors operated without the benefit of a significant overburden. This reduction is achieved by selecting narrow coincidence windows following POT. Including a 10 μs allowance for the arrival of delayed $\bar{\nu}_\mu$ and ν_e (Sec. I) this background reduction is by a factor of 2.5×10^{-4} at J-PARC MLF. This derives from the beam duty cycle described in the previous section. Additionally, steady-state backgrounds can be characterized at times preceding POT. This allows their subtraction from the energy spectrum of POT-coincident signals, leaving only the contributions from CEνNS and any beam-related backgrounds. Following their dedicated *in situ* characterization previous to CEνNS experimentation [2, 3], beam-related backgrounds can be diminished to a negligible level by careful shielding of the detectors. For instance, a fraction of highly-energetic (hundreds of MeV) prompt neutrons can escape the shielding monolith around the spallation target to reach the detector within POT-coincident windows. Even if the time structure of their signals is not identical to that expected from CEνNS, proper shielding and/or vetoing of the background they induce is of the essence. In order to evaluate the potential at J-PARC of the detector technologies described in the next section, Geant4 [30] and MCNPX [28] simulations were used to compare various expected background sources with the calculated rate of CEνNS events. The backgrounds considered and the specific input to the simulations are as follows:

1. environmental neutrons

Environmental neutrons (cosmic-ray tertiaries and those from fission decays and (α, n) reactions) contin-

uously affect detectors not benefiting from a significant overburden as is the case for experimental sites in close vicinity to spallation sources. We adopt their spectral hardness as described in [31, 32]. Their thermal and epithermal fluxes do not appreciably contribute to the backgrounds in the devices considered here, for the shielding assumed. Fast neutrons (0.1 - 20 MeV) are simulated assuming an isotropic origin. An ultra fast component (20 MeV - 1 GeV) is simulated with an origin biased skyward [33]. The supplementary flux via (n,Xn) reactions that energetic neutrons can produce in shielding (primarily in lead) is included in our simulations.

2. **internal radiopurity**

The intrinsic radioactive backgrounds affecting each detector technology are simulated using Geant4 [30]. PPC germanium detectors are the exception, as this steady-state background is available to us as a measurement, in conditions of negligible overburden as expected at J-PARC MLF. Contributions from the full decay chains of the various radioactive impurities are scaled by activities derived from the screening of detector materials. Those contributions are reduced by suitable cuts (e.g., coincidences between multiple detector elements or with active vetoes, as in the case for CsI).

3. **muon-induced neutrons**

Muons at Earth (cosmic-ray secondaries) traversing the detector and shielding geometries engender tertiary neutrons that can in turn produce nuclear recoil events in the same energy region as CEνNS signals. These neutrons are simulated as homogeneously produced in the lead shielding of each detector, with a hardness following [34, 35]. Their contribution is diminished by the measured tagging efficiency (typically $> 99.9\%$) of an external muon veto surrounding the geometry.

4. **beam-related neutrons**

As mentioned, directly competing with the CEνNS signal are POT-coincident neutron-induced signals from energetic neutrons escaping the shielding monolith around the spallation target. Taking the overall neutron flux measured at the SNS as a reference [2, 3], scaled up for J-PARC's expected power delivery of 1.3 MW and the higher yield of neutrons from 3 GeV protons, simulations similar to those described in [6, 36] were performed to find the background those induce in the detectors considered. A power law approximation as in [37, 38] describes the hardness of their spectrum in the third floor terrace of the MLF.

5. **neutrino-induced neutrons (NINs)**

The second directly competing signal to CEνNS arises from the charged-current interaction $^{208}\mathrm{Pb}(\nu_e, e^- Xn)$ in the lead surrounding each detector. Homogeneously distributed origins and an isotropic emission are adopted, with an spectral hardness derived from [39], which is nearly identical to that used in [2, 3]. The neutron production rate from [40] is scaled to the $\sim 2.58 \times 10^7$ $\nu_e/\mathrm{cm}^2/\mathrm{s}$ expected 20 m away from the J-PARC MLF mercury target, with a multiplicative correction by a factor of 0.29 applied to account for the upper limit to this reaction imposed in [41].

IV. DETECTOR TECHNOLOGIES

A. Cryogenic CsI

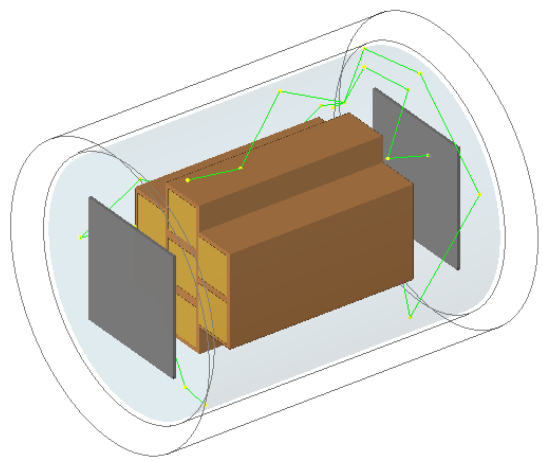

FIG. 2. Rendition of the Geant4 geometry for the cryogenic CsI detector. Seven CsI crystals within OFHC copper holders, the LAr volume around them (gray), and two (dark gray) 20 × 20 cm SiPM tiles [42] are visible. Also shown is an example track by a LAr scintillation photon originating from a background event, wavelength-shifted and reflected towards the SiPM panels (see text).

This detector, conceptually described in [18] and depicted in Fig. 2, is a compact 44 kg array of seven cryogenically-operated pure (i.e., undoped) CsI crystals submerged in a liquid argon (LAr) bath. Similar designs using this same scintillating material have been proposed by others [43, 44]. The QF for this material in the energy region relevant to CEνNS has been recently measured [45, 46]. Each crystal has dimensions of $6.6 \times 6.6 \times 32$ cm. A low-noise, high-efficiency large area avalanche photodiode (LAAPD, [47]) on each end reads out the scintillation light produced by radiation interactions in the CsI scintillator. The LAr bath doubles as thermal control —maintaining temperature in the regime that provides a maximum light yield from this material [45] and best LAAPD performance [46]— and as an active internal veto against neutrons able to penetrate the passive shielding surrounding the detector. This consists of 15 cm of Pb, 30 cm of polyethylene, and 5 cm of plastic scintillator (muon veto).

The modular segmentation of the CsI crystal array assists in background event rejection, whether beam-

related or steady-state, via coincidence cuts. For purposes of this simulation, a layer of tetraphenyl butadiene (TPB) waveshifter coating a Tetratex reflector [48] is assumed to cover all surfaces inner to the LAr volume. Its conversion efficiency and emission properties [49] were used for optical simulations mapping the position-dependent efficiency of this inner veto to waveshift and transport LAr scintillation light into two submerged large-area silicon photomultiplier (SiPM) arrays. SiPMs like those described at [42, 50] have a sufficiently-low dark count rate in cryogenic conditions to allow operation of two 20 × 20 cm tiles like those in Fig. 2 at single photoelectron sensitivity, while causing only a modest (few percent) dead time.

	Amcrys CsI[Na]	SICCAS CsI
Th-232	< 0.5	0.03
U-238	2.4	0.09
K-40	16.7	< 4.1
Cs-137	27.9	1.3
Cs-134	25.9	33
Rb-87	38 ppb	1.8 ppb

TABLE I. Radiopurity of the CsI[Na] scintillator used for [2, 3] and the SICCAS stock being considered for the cryogenic CsI array (units of mBq/kg except for Rb-87). Cs-134 is a result of thermal neutron activation, i.e., expected to be invariant at equilibrium.

Order-of-magnitude improvements in the radiopurity of commercially-available CsI stock from SICCAS [51] (Table I) results in a background contribution of just ~ 30 counts/keV-kg-day from this internal source before the reduction derived from beam duty-time. Measurements made by the manufacturer and at SNOLAB's Low Background Counting Facility, shown in Table I, illustrate the improvements fed into present simulations.

Fig. 3 aggregates the contributions of the various background sources simulated, comparing them to the expected CEνNS rate. The steady-state backgrounds shown in the left panel of Fig. 3 can be subtracted via their characterization during the 10 μs prior to the POT trigger [2, 3]. Beam-coincident backgrounds are rendered subdominant to the CEνNS signal with the active and passive shielding layers assumed here.

We adopt a conservative energy threshold of 4.5 keVnr for this detector, which derives from the rapid decrease in the low-energy QF observed in Ref. [45].

B. Ge PPC

A large-mass (3 kg) p-type point-contact (PPC, [53]) germanium detector considered here is an upgraded design currently in operation at the Vandellòs-II nuclear power plant. Its shielding structure is identical to that described in [54], consisting of a 5 cm inner active veto (plastic scintillator), 15 cm of Pb (innermost 2.5 cm low in Pb-210), and a 5 cm outer muon veto. Attention has been paid to the radiopurity and cleaning of internal PPC components and those in the inner veto, achieving a background level of 25 counts/keV-kg-day at 0.2 keV$_{ee}$ under a shallow 6 m.w.e. overburden [18] ("ee" refers to "electron equivalent", i.e., ionization energy). This available measurement of the steady-state background takes the place of a dedicated simulation for purposes of present estimates.

Fig. 4 shows the background in the Ge detector, simulated and measured, in comparison to the expected CEνNS rate. Roughly an order of magnitude higher signal than background rate is expected at threshold. The ease of the addition of an external neutron moderator such as polyethylene, not included in the present simulation, makes this a conservative estimate of the prompt neutron-induced background. The steady-state backgrounds are subtractable by comparing data coincident with beam spills with data in the periods prior, as for CsI.

We adopt an energy threshold of 0.3 keVnr. This derives from the lowest-detectable ionization signal in a modern PPC benefiting from an external trigger, when a 20% QF is adopted as a compromise between the values postulated in Refs. [10, 11].

C. Gaseous TPC

Noble gases Time Projection Chambers (TPCs) with electroluminescent amplification is a technology that has revolutionized Dark Matter searches in the last 20 years by allowing for a large exposure with high sensitivity to low energy depositions in the active volume thanks to its intrinsic signal amplification. In this case the GanESS collaboration proposes to use a single-phase high-pressure gas electroluminescent TPC providing the capability to change between different noble gases operation with no modification of the detector. The high pressure gas TPC is a technology that has been largely developed for neutrinoless double beta decay searches within the NEXT Collaboration [55] and can be extended to low energy searches. In addition, the use of gas TPC has the advantage of allowing for signal amplification without the issues of "spontaneous" single electron signals that often follow a large event that limits the surface operation of dual-phase detectors. Also, in comparison with single phase detectors, the amplification capabilities will allow for an improved energy threshold. For concreteness, we assume the same energy threshold and QF as in Ref. [18].

Fig. 5 shows a transverse cut of the design of the GanESS detector, with two symmetric TPCs of 30 cm drift length and 60 cm diameter with a common cathode. The two TPCs are placed inside a stainless steel 316Ti radio-pure alloy that allows the detector to operate above 35 bar. Two electroluminescent regions are responsible for the signal amplification in each side of

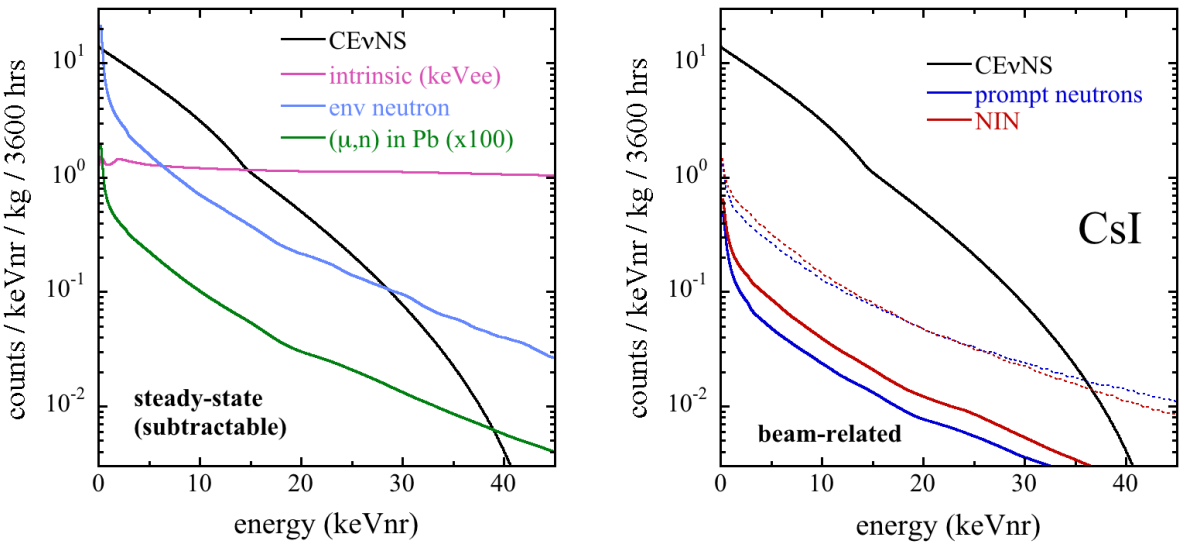

FIG. 3. *Left:* Subtractable steady-state backgrounds induced in the CsI detector array alongside the expected CEνNS rate. The reduction in magnitude for these backgrounds due to beam duty time at J-PARC MLF is applied here. To convert the intrinsic background to keVnr, we assume an 8% QF [45]. *Right:* Beam-associated backgrounds (non-subtractable) in comparison to the expected CEνNS signal. Dotted lines indicate their magnitude prior to applying LAr inner veto cuts.

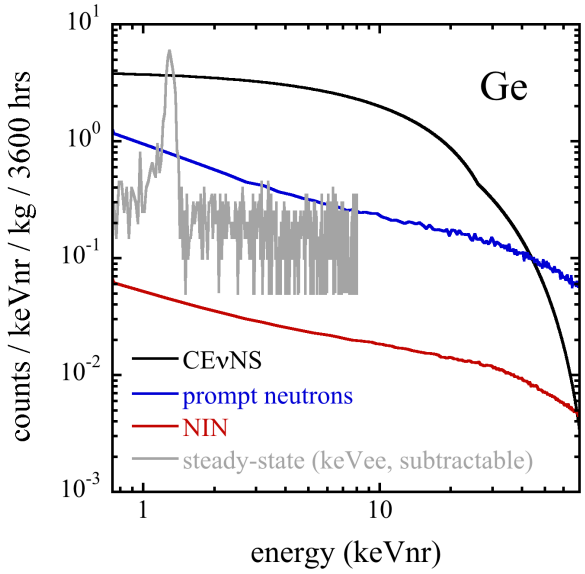

FIG. 4. Beam-associated (non-subtractable) and subtractable steady-state backgrounds in comparison to the expected CEνNS signal in the Ge detector (see text). The steady-state component is reduced by the beam duty time and expressed in per keV$_{ee}$ units. For a more direct comparison, the rest of spectra can be converted to the same energy scale using the QF for germanium, that we set to 20% in our simulations [52].

the detector. That signal is read by a plane of 19 Hamamatsu R11410-20 3 inch PMTs just behind the amplification region. These PMTs are protected from the pressure volume by an 8 mm thick sapphire window sealed with a steel frame. The windows are coated with a resistive polymer (PEDOT) to guarantee proper grounding on the surface and prevent any field leakage into the PMT. On top of the polymer, we added a coating of tetraphenyl butadiene (TPB) to transform the VUV light emitted by noble gases into blue light, for which sapphire is not opaque. In addition, the inner walls of the TPCs are covered by teflon panels also coated with TPB to maximize light collection. The GanESS detector will use the vessel and PMTs employed for the NEXT-White detector [56] where all materials were screened and characterized for neutrinoless double-beta decay searches [57].

In this technology, the time resolution for the amplified signal is limited to the total time drift of the whole active volume ($\sim$300 μs in this case). If the drift time can be determined, the time resolution can then be of only a few nanoseconds. There are two different possibilities for determining the total drift distance: detection of the primary scintillation signal and measuring the electron diffusion, which is proportional to the square root of the drift time. In the case of very low energy signals, measuring the diffusion is complicated due to the limited number of ionised electrons. Fig. 6 shows the error on the estimation of the z-position as a function of the interaction distance to the amplification region for different recoil energies. It can be observed that this method is not particularly good as the error becomes larger than tens of millimetres in almost any situation, which will translate into tens of microseconds. On the other hand, for a system operated with PMTs with negligible dark count, identification of single photons is possible. In this case, the observation of a signal of 1 or 2 photons in the PMT plane in the time window between the arrival

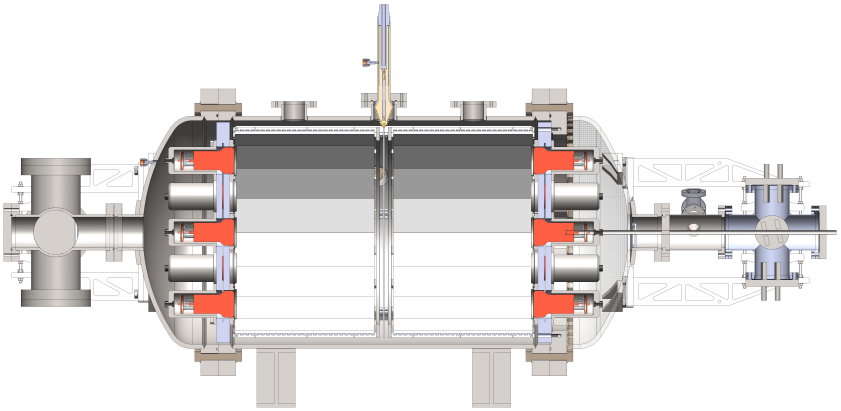

FIG. 5. Lateral cut of the GanESS detector design, consisting of two symmetrical TPCs with the cathode in the center of a stainless steel 316Ti alloy vessel, allowing for operation above 35 bar. Two planes of 19 PMTs each read both the primary scintillation light produced by the events and the amplified signal of the ionised electrons when crossing the electroluminescent regions in the laterals of the detector. This detector allows for operation with any noble gas, in particular argon and xenon which are the gases assumed in this work.

of the pulse and the amplified signal will be associated to the detection of the primary scintillation signal. Fig. 6 bottom shows the detection probability of more than one and more than 2 photons in a time window of 100 ns as a function of the nuclear recoil energy. As can be seen in this plot, we obtain moderate efficiencies even at low energies. In addition, in light of the relevance of the time information for the physics case of this process (see Sec. V), the detector could be designed for an improved collection of the primary signal.

The main backgrounds affecting this technology are the ones described in Sec. III with an important difference between the operation with xenon and argon, as natural argon includes the ^{39}Ar isotope that introduces a constant and flat background in the region of interest at the level of 14.6 evt/keV/kg/year, which is the dominant contribution coming from inner components. Initial simulations of the background events produced by beam-related neutrons include two layers of passive shielding, 30 cm of polyethylene with an inner layer of 15 cm of lead. These simulations produce an almost flat spectrum at the level of 2 evt/keV/kg/year. The time dependence of this background has also been implemented taking into account the time profile of the J-PARC beam with two pulses separated by 540 ns.

V. PHYSICS REACH

A precision measurement of CEνNS provides a direct probe of both SM and beyond the standard model (BSM) physics. Paradigmatic examples of the former are the determination of the weak mixing angle at very low momentum transfer [58–65] and the study of nuclear structure [63–69]. The program of BSM exploration with CEνNS is broad (see, e.g., Refs. [18, 61, 70–119] for an incomplete list), being most sensitive to a variety of scenarios leading to modified neutrino interactions with nuclei — in particular at low momentum transfer — but extending also to the production of new light neutral states and sterile neutrino searches, among others.

In what follows we illustrate, for a variety of target nuclei and detection technologies, the potential sensitivity of a CEνNS experiment at J-PARC to SM and BSM physics: the weak mixing angle, neutrino charge radius, neutron radius, non-standard neutrino interactions (NSI), new neutral interactions with light-mediators, anomalous neutrino magnetic moment, and eV-scale sterile neutrinos.

A. Parameters and assumptions used in the calculations

All sensitivity calculations in this work are obtained by binning the observed events in reconstructed nuclear recoil energy, $T^{\rm r}$ (after accounting for the effect of the QF on the detector threshold and backgrounds, and taking the QF uncertainty into account) and reconstructed time, $t^{\rm r}$. Table II summarizes the detector properties assumed in the simulation. For the HPGe (high-purity germanium) PPC and Cryogenic-CsI detectors we assume that time can be reconstructed for all events. For TPCs, we distinguish two event samples. On the one hand, *S1 events*, where the prompt scintillation light is detected, allowing to reconstruct the interaction time with good accuracy as described in Sec. IV C. These occur with probability $\epsilon_t(T)$, obtained from detector simulation (see

Detector Technology	Target nucleus	Mass (kg)	Energy Thres. ($\equiv T_{\rm th}$, keV$_{\rm nr}$)	Energy Resol. at $T_{\rm th}$ ($\equiv \sigma_{T,0}$, %)	Time Resol. ($\equiv \sigma_t$)		CEνNS $\frac{\rm NR}{\rm yr}$	BR bck $\frac{\rm NR}{\rm yr}$	NiN bck $\frac{\rm NR}{\rm yr}$	SS bck $\frac{\rm NR}{\rm yr}$
Cryogenic scintillator	CsI	44	4.5	30	0.7234 ln(ns)		1296	12	25	961
p-type point contact HPGe	Ge	7	0.3	15	85 ns		225	64	3.8	33
High-pressure gaseous TPC	Xe	20	0.9	40	S1 events	100 ns	253	25	negl.	negl.
					NoS1 events	–	823	39		
High-pressure gaseous TPC	Ar	6	0.9	40	S1 events	100 ns	80	69	negl.	623
					NoS1 events	–	40	99		894

TABLE II. Summary of detector properties used in our sensitivity calculations.

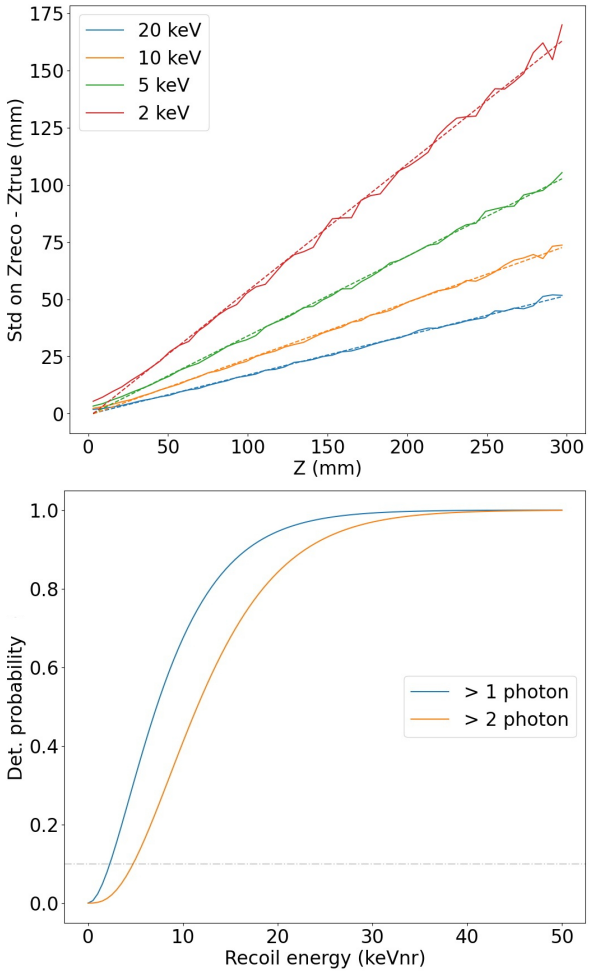

FIG. 6. Top: Error on the reconstruction of the z-position of events at different energies as a function of their distance to the amplification region for the case of a high-pressure gaseous xenon detector (see text). Bottom: Detection probability of the primary scintillation light of more than 1 or 2 photons as a function of the nuclear recoil energy also calculated for xenon operation. A horizontal line represents 10% detection probability.

Sec. IV C and Fig. 6). We conservatively include only events with more than 2 scintillation photons. This suppresses the number of events with time discrimination at low recoil energies. On the other hand, *NoS1 events*, where the prompt scintillation light is not detected and for which the interaction time cannot be constructed. These occur with probability $1-\epsilon_t(T)$.

The double differential predicted number of signal events in the reconstructed variables reads

$$\frac{{\rm d}^2 N^{\rm S}}{{\rm d}T^{\rm r}\,{\rm d}t^{\rm r}} = \int_0^{t_{\rm max}} {\rm d}t \int_{T_{\rm th}}^{\infty} {\rm d}T\, \frac{{\rm d}^2 N^{\rm S}}{{\rm d}t\,{\rm d}T} R_T(T^{\rm r},T) R_t(t^{\rm r},t)\epsilon_t(T)\,, \tag{5.1}$$

where $\frac{{\rm d}^2 N}{{\rm d}t\,{\rm d}T}$ is the distribution of events in true time, t (we set $t=0$ when protons hit the target); and true nuclear recoil energy, T. $R_T(T^{\rm r},T)$ and $R_t(t^{\rm r},t)$ are the corresponding energy and time resolution functions. $\epsilon_t(T)=1$ for HPGe PPC and Cryogenic-CsI. For TPCs the above expression is valid for S1 events, while for NoS1 events we only bin in reconstructed energy

$$\frac{dN^{\rm S,NoS1}}{dT^{\rm r}} = \int_0^{t_{\rm max}} dt \int_{T_{\rm th}}^{\infty} dT\, \frac{d^2 N^{\rm S}}{dtdT} R_T(T^{\rm r},T)[1-\epsilon_t(T)]\,. \tag{5.2}$$

For all detectors we assume Gaussian smearing of the reconstructed recoil energy around the true one, with an energy-dependent width $\sigma_T(T) = \sigma_{T,0}\sqrt{T/T_{\rm th}}$, where $\sigma_{T,0}$ is the energy resolution at the detection threshold ($T_{\rm th}$) listed in Table II. As for the time resolution, for both the HPGe PPC and the S1 events in TPCs we assume Gaussian smearing of the reconstructed time around the true one —the latter spanning from $t=0$ to $t=t_{\rm max}=\infty$—, with a constant width σ_t given in Table II. For the Cryogenic-CsI detector we find the time resolution to be better described by a lognormal distribution of $(t^{\rm r}-t)$ —so $t_{\rm max}=t^{\rm r}$— centered at $\mu=2.578$ and with $\sigma=0.7234$, both in ln (ns).

For all scenarios considered the true event distribution can be always factorized as

$$\frac{d^2 N^S}{dtdT} = \sum_{X=\nu_e,\nu_\mu,\overline{\nu}_\mu} f_{t,\,X}(t) g_X(T) \tag{5.3}$$

where $f_{t,\,X}(t)$ describes the time distribution (normalized to 1 for convenience) of the neutrinos with flavour X arriving at the detector. As described above, neutrinos are produced from pion decay $\pi^+ \to \mu^+ + \nu_\mu$, and

subsequent muon decay $\mu^+ \to e^+ + \nu_e + \bar{\nu}_\mu$; with both decays happening at rest. Since pions are produced instantaneously when protons hit the target (as mentioned above, we set that time to be $t = 0$) one can obtain the neutrino time distributions as

$$f_{t,\nu_\mu}(t) = \int_0^t \mathrm{d}t' \, \frac{\mathrm{d}n_p}{\mathrm{d}t'}(t') \frac{e^{\frac{t'-t}{\tau_\pi}}}{\tau_\pi} \,, \tag{5.4}$$

$$f_{t,\nu_e}(t) = f_{t,\bar{\nu}_\mu}(t) = \int_0^t \mathrm{d}t' \, \frac{\mathrm{d}n_p}{\mathrm{d}t'}(t') \frac{e^{\frac{t'-t}{\tau_\mu}} - e^{\frac{t'-t}{\tau_\pi}}}{\tau_\mu - \tau_\pi} \,, \tag{5.5}$$

where τ_π and τ_μ are the pion and muon lifetimes, respectively. $\mathrm{d}n_p/\mathrm{d}t$ is the time profile of the proton beam, which as mentioned above at J-PARC consists of square pulses of 100 ns separated by 540 ns [24]. Explicitly,

$$\frac{\mathrm{d}n_p}{\mathrm{d}t} = \begin{cases} 0 & \text{if } t < 0 \\ 5\,\mu\mathrm{s}^{-1} & \text{if } 0 < t < 0.1\,\mu\mathrm{s} \\ 0 & \text{if } 0.1\,\mu\mathrm{s} < t < 0.54\,\mu\mathrm{s} \\ 5\,\mu\mathrm{s}^{-1} & \text{if } 0.54 < t < 0.64\,\mu\mathrm{s} \end{cases} \,, \tag{5.6}$$

where we have normalized the time distribution to 1.

The time distributions $f_{t,X}(t)$ are the same for all the scenarios considered, so that all model-dependence is in the energy-dependent functions $g_X(T)$ given by:

$$g_X(T) = \varepsilon \, \frac{N_p f_{\nu/p} N_t}{4\pi\ell^2} \int_{E_\nu^{\min}}^{\infty} \mathrm{d}E_\nu \, \phi_X(E_\nu) \frac{\mathrm{d}\sigma_X}{\mathrm{d}T}(E_\nu, T) \,, \tag{5.7}$$

where $E_\nu^{\min} = \left(T + \sqrt{T^2 + 2TM}\right)/2$ is the minimum neutrino energy that can generate a nuclear recoil energy T, with M the mass of the target nucleus. $\phi_X(E_\nu)$ is the normalized neutrino flux of flavour X

$$\phi_{\nu_\mu} = \delta\left(E_\nu - \frac{m_\pi^2 - m_\mu^2}{2m_\pi}\right) \,, \tag{5.8}$$

$$\phi_{\nu_e} = \frac{96}{m_\mu^4}(m_\mu E_\nu^2 - 2E_\nu^3)\,\theta\left(\frac{m_\mu}{2} - E_\nu\right) \,, \tag{5.9}$$

$$\phi_{\bar{\nu}_\mu} = \frac{16}{m_\mu^4}(3m_\mu E_\nu^2 - 4E_\nu^3)\,\theta\left(\frac{m_\mu}{2} - E_\nu\right) \,. \tag{5.10}$$

m_μ and m_π are the pion and muon masses, and θ is the Heaviside step function, that cuts the latter two distributions at $E_\nu = m_\mu/2$.

The normalization factors in Eq. (5.7) include the detection efficiency, ε; the number of pions per proton, $f_{\pi/p}$; the source-target distance, ℓ; the number of target nuclei, N_t; and the number of protons on target, N_p. The latter is determined by the beam power, P; the proton energy, E_p; and the running time, t_{run}; as $N_p = \frac{P}{E_p} \times t_{\mathrm{run}}$. Unless otherwise stated, a common set of assumptions apply to these normalization factors, for all detector configurations considered in this work:

1. The beam power is assumed to be 1.3 MW and the proton energy 3 GeV, as discussed in Sec. I. We assume 3 years of running time and an exposure of 3,600 hr per calendar year due to periods of maintenance at the facility [120–122]. Thus

$$N_p \simeq 3.5 \cdot 10^{22} \left(\frac{P}{1.3\,\mathrm{MW}}\right)\left(\frac{3\,\mathrm{GeV}}{E_p}\right)\left(\frac{t_{\mathrm{run}}}{\mathrm{yr}}\right) \,.$$

2. We assume $f_{\pi/p} = 0.44$, as discussed in Sec. II.

3. The detector distance to the target is set to 20 m. A number of possible detector locations can be envisioned at this distance within the third floor terrace of the MLF [37, 38].

4. The detection efficiency is assumed to be a step function at threshold, with a conservative 80% acceptance.

In the SM, the differential cross section for CEνNS of ν_α on a nucleus of mass M consisting of Z protons and N neutrons reads [1]:

$$\frac{d\sigma^\alpha}{dT} = \frac{G_F^2}{2\pi}\frac{\mathcal{Q}_{W,\alpha}^2}{2}|F(Q^2)|^2 M\left[1 - \frac{MT}{2E_\nu^2} - \frac{T}{E_\nu} + \frac{T^2}{2E_\nu^2}\right] \,, \tag{5.11}$$

where E_ν is the incident neutrino energy, G_F is the Fermi constant, and

$$\mathcal{Q}_{W,\alpha} = -N + Z\left[1 - 4\sin^2\theta_W(1 + \Delta_\alpha)\right] \tag{5.12}$$

is the weak charge of the target nucleus with θ_W the Weinberg angle that, for the sake of concreteness, in our SM calculations has been set to its value at zero momentum transfer $\sin^2\theta_W = 0.23867$ [123]. In Eq. (5.12) we have introduced the flavour-dependent factor $\Delta\alpha$, which in the SM is directly related to the effective neutrino charge radius, $\langle r_\nu^2 \rangle$ [124] defined as

$$\langle r_\nu^2 \rangle \equiv -6\frac{dF_\nu^{\mathrm{em}}(Q^2)}{dQ^2}\bigg|_{Q^2=0} \,, \tag{5.13}$$

where F_ν^{em} is the electromagnetic form factor of the neutrino. The inclusion of this form factor affects the scattering of neutrinos with other charged particles and effectively induces a flavour-dependent shift [125–127],

$$\Delta_\alpha = \frac{1}{3}m_W^2\langle r_{\nu_\alpha}^2 \rangle \tag{5.14}$$

where m_W is the mass of the W boson. The value of the neutrino charge radius in the SM [128–130] is

$$\langle r_{\nu_\alpha}^2 \rangle = \frac{-G_F}{2\sqrt{2}\pi^2}\left[3 - 2\ln\left(\frac{m_{\ell_\alpha}^2}{m_W^2}\right)\right] \,, \tag{5.15}$$

with m_{ℓ_α} the mass of the charged lepton of flavour α. In Eq. (5.11), $F(Q^2)$ is the weak form factor of the nucleus evaluated at the squared momentum transfer of the process, $Q^2 = 2MT$, which we parametrize as [131]

$$F(Q^2) = 3\frac{j_1(QR_0)}{QR_0}e^{-\frac{Q^2 s^2}{2}} \tag{5.16}$$

with j_1 being the spherical Bessel function, $R_0^2 \equiv \frac{5}{3}(R_W^2 - 3s^2)$, R_W the weak radius of the nucleus

$$R_W^2 \equiv -6 \frac{dF(Q^2)}{dQ^2}\bigg|_{Q^2=0}, \tag{5.17}$$

and $s = 0.9\,\text{fm}$ the neutron skin. As CEνNS happens at low momentum transfers, only the low-Q^2 values of the form factor are phenomenologically relevant, and other parametrizations of $F(Q^2)$ with the same weak radius would lead to very similar results.

R_W can be expressed in terms of the nuclear charge radius (R_{ch}), the point-proton and neutron distribution radius (R_p^{pt} and R_n^{pt}), and the proton and neutron square charge radius ($r_{\text{ch},\,n}$ and $r_{\text{ch},\,p}$) as [69]

$$R_W^2 = R_{\text{ch}}^2 + \frac{N}{Q_W}\left[(R_n^{\text{pt}})^2 - (R_p^{\text{pt}})^2 + \frac{Z^2-N^2}{ZN} r_{\text{ch},\,n}^2\right] \tag{5.18}$$

with $(R_p^{\text{pt}})^2 \equiv R_{\text{ch}}^2 - r_{\text{ch},\,p}^2 - \frac{N}{Z} r_{\text{ch},\,n}^2$. In our calculations we use as inputs the tabulated nuclear charge radii from Ref. [132], together with the Particle Data Group (PDG) [133] values for the squared proton and neutron charge radii: $r_{\text{ch},\,p}^2 = 0.707\,\text{fm}^2$ and $r_{\text{ch},\,n}^2 = -0.1161\,\text{fm}^2$. For the sake of concreteness, in our simulations we generate the expected number of events by setting the point neutron radius to be the best fit value of the fit in Ref. [134], $R_n^{\text{pt,true}} = R_p^{\text{pt}} - 0.04 + 1.01N - Z/A$.

The CEνNS cross section depends on the target nuclear isotope. For Xe, Ge, and Ar, we use their natural isotope abundances as taken from Ref. [135]. For the CsI detector we assume a 50% number abundance of Cs and 50% of I. For convenience, the values of R_{ch} (and hence R_p^{pt}) as well as the assumed true value of $R_n^{\text{pt,true}}$ used in our calculations are summarized in Tab. III.

Target	Z	N	%	R_{ch} (fm)	R_p^{pt} (fm)	$R_n^{\text{pt,true}}$ (fm)
Xe	54	78	26.9	4.786	4.729	4.873
		75	26.4	4.778	4.720	4.844
		77	21.2	4.780	4.724	4.861
		80	10.4	4.780	4.734	4.890
		82	8.9	4.796	4.741	4.909
		76	4.1	4.782	4.725	4.885
		74	1.9	4.777	4.720	4.837
Ar	18	22	100	2.427	2.308	2.369
Ge	32	42	36.7	4.074	4.005	4.102
		40	27.3	4.058	3.988	4.060
		38	20.4	4.041	3.970	4.017
		44	7.8	4.081	4.013	4.133
		41	7.8	4.063	3.994	4.078
CsI	55	78	50	4.750	4.692	4.819
	53	74	50	4.804	4.747	4.882

TABLE III. Main properties of the nuclei/molecule for the different targets considered in this work. The different columns indicate the isotope considered and their abundance together with the number of protons and neutrons, the nucleus charge radius, the point proton distribution radius, and the true point neutron distribution radius assumed in the simulations.

In what respects the expected backgrounds, they can be divided into three classes (see Sec. III for more details): (i) steady-state backgrounds (SS bck); (ii) beam-related backgrounds (BR bck), produced by neutrons escaping the target monolith and reaching the detector; and (iii) neutrino-induced neutrons (NiN bck). For each of the detectors considered the time and energy dependence of these three backgrounds have been estimated as discussed in Sec. IV. For illustration we list in table II the total number of expected CEνNS events and of the three considered backgrounds per run year (including the 80% detection efficiency). It is important to notice that, while the steady-state background can be in principle sizable, it can be efficiently measured using beam-off data and therefore can be subtracted leaving only the residual statistical uncertainty associated to the subtraction process.

As described in Sec. II, the pulsed nature of the J-PARC proton beam provides a unique handle to discriminate BSM flavour-dependent scenarios. To illustrate this, we plot in Fig. 7 the predicted distribution of events as a function of the reconstructed recoil energy, T^{r}; and the reconstructed time, t^{r}; in the Cryogenic-CsI detector (with the steady-state background subtracted) for three years of run time. The figure clearly displays how the relative weight of ν_e-induced and ν_μ-induced event substantially changes with the time of the event. To this end, the distribution is shown for the SM as well as for an NSI scenario (see below for definitions) which leads to almost the same total number of events. As seen in the left panel, the recoil energy distribution does not allow to discriminate this model from the SM. On the contrary, as seen on the right panel, with the time information this scenario can be tested with high confidence.

Altogether, in order to determine the sensitivity to a model characterized by a set of parameters $\{\varepsilon\}$, we build a bi-dimensional binned χ^2. Systematic uncertainties are implemented using the pull method. We consider three sources of systematic uncertainties which we assume to be fully correlated among the bins: 10% uncertainty for the flux normalization —see the discussion in Sec. II— , an achievable 5% uncertainty on the QF [45, 136]— equivalent to an energy-scale uncertainty— (pull ξ_{QF} with $\sigma_{QF} = 0.05$), and 5% uncertainty on the normalization of the irreducible beam-related and neutrino-induced-neutron backgrounds (pull ξ_B with $\sigma_B = 0.05$). We have verified that including two different pulls for these two backgrounds leads to very similar results.

With this, for HPGe PPC and Cryogenic-CsI detectors and for the S1 TPC events, we construct:

$$\chi^2(\{\varepsilon\}) = \min_\xi \left[\chi^2(\{\varepsilon\},\xi) + \sum_{p=F,QF,B}\left(\frac{1-\xi_p}{\sigma_p}\right)^2\right], \tag{5.19}$$

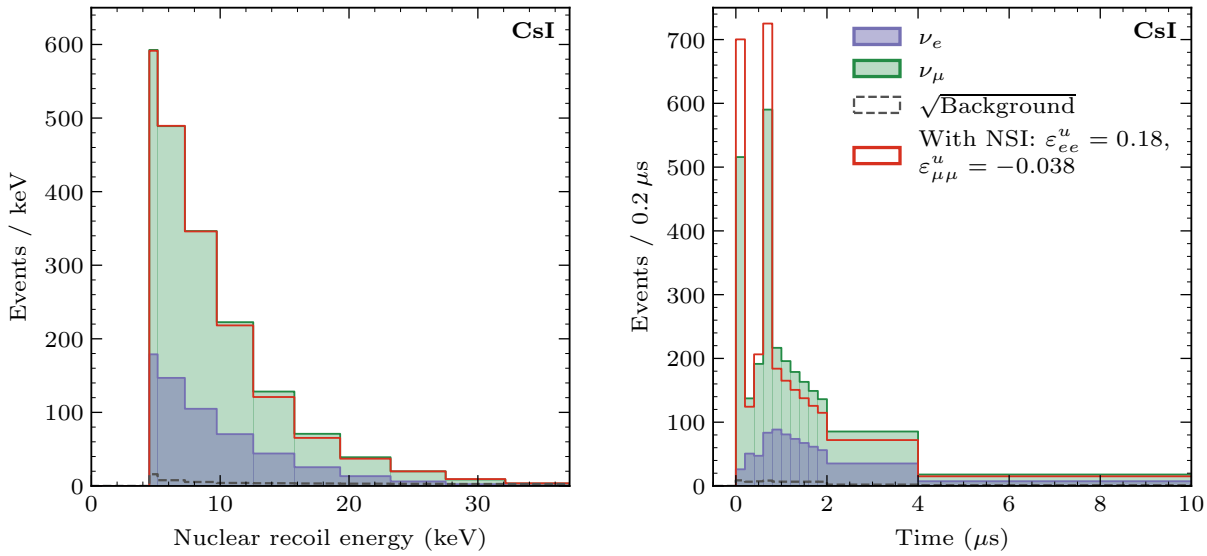

FIG. 7. Predicted event distribution as a function of the reconstructed recoil energy, $T^{\rm r}$, and the reconstructed time $t^{\rm r}$ in the Cryogenic-CsI detector (with the steady-state background subtracted) for three years of run time. The distributions are shown for the SM and for an example of NSI scenario (see below for definitions). The binning shown is the one employed in the analysis for this detector and it has been chosen to ensure enough events when binning in both variables.

where

$$\chi^2(\{\varepsilon\},\xi) = \sum_{ij} 2\Big[\quad N_{ij}(\{\varepsilon\},\xi) - \overline{N}_{ij} + \overline{N}_{ij} \ln\left(\frac{\overline{N}_{ij}}{N_{ij}(\{\varepsilon\},\xi)}\right)\Big]. \tag{5.20}$$

$N_{ij}(\{\varepsilon\},\xi)$ are the predicted number of events with reconstructed time $\in [t^{\rm r}_i, t^{\rm r}_{i+1}]$ and reconstructed nuclear recoil energy $\in [T^{\rm r}_j, T^{\rm r}_{j+1}]$ for the model to be tested,

$$N_{ij}(\{\varepsilon\},\xi) = \xi_F \int_{t^{\rm r}_i}^{t^{\rm r}_{i+1}} dt^{\rm r} \int_{\xi_{QF} T^{\rm r}_j}^{\xi_{QF} T^{\rm r}_{j+1}} dT^{\rm r} \frac{d^2 N^S}{dt^{\rm r} dT^{\rm r}}(\{\varepsilon\}) + N^{\rm bck}_{{\rm SS},ij} + \xi_B (N^{\rm bck}_{{\rm BR},ij} + N^{\rm bck}_{{\rm NiN},ij}) \,. \tag{5.21}$$

$\overline{N}_{ij}$ stands for the *data* event rates which we assume to be the rates expected in that bin from the combination of signal and background in the SM with $\xi_i = 1$, and for the assumed true values of the SM parameters. We notice that in Eq. (5.21) we do not include any systematic background pull for the steady-state background since, as mentioned above, we assume that this background can be independently measured using beam-off data, and therefore subtracted, so we account only for its effect on the statistical uncertainty.

In addition, for high pressure TPC detectors we add the corresponding χ^2 for the NoS1 events which is only binned in $T^{\rm r}$.

B. Weak mixing angle and neutrino charge radii

The weak mixing angle is a fundamental parameter in the SM whose scale dependence in a given renormalization scheme is predicted within the model, with a precision of 2×10^{-5} [123], to become approximately constant at scales below $\mathcal{O}(0.2)$ GeV. Experimentally, it has been most precisely measured at the electroweak scale in collider experiments [133], with $\mathcal{O}(10^{-3})$ or better accuracy. This sets the target precision for low-energy experiments to provide a test of the model. Below GeV scales, $\sin^2\theta_W$ has been determined at ~ 0.2 GeV in measurements of the parity-violating asymmetry in Moller scattering [137] and electron-proton scattering [138] with ~ 0.5 % precision, and at ~ 2.4 MeV in measurements of parity violation in Cs atoms [139, 140] with ~ 0.8 % precision. CEνNS provides also a low-energy measurement of $\sin^2\theta_W$, with the most precise determination so far provided by the COHERENT measurement of CEνNS on CsI, $\sin^2\theta_W = 0.220^{+0.028}_{-0.026}$ (1σ) [141].

Our results on the expected sensitivity for this parameter are shown in Table IV for the different detectors under consideration. As seen in the table, any of the experiments considered here leads only to a mild improvement on the determination of the weak mixing angle in CEνNS with respect to the current COHERENT result, all being still far from the precision of atomic parity violation experiments. This is so, because, as seen in Eq. (5.11), the weak mixing angle enters the CEνNS cross section through the coupling with protons Z in the weak charge Q_W, leading only to an overall normalization correction to the total number of expected events. Consequently,

	CsI	Ge	Xe	Ar
$\sin^2\theta_W$	$0.239^{+0.033}_{-0.026}$	$0.239^{+0.031}_{-0.025}$	$0.239^{+0.033}_{-0.027}$	$0.239^{+0.037}_{-0.033}$
$\langle r^2_{\nu_e}\rangle$ (10^{-32}) cm^2	$[-54., -48.3] \oplus [-3., 2.1]$	$[-42., -36.6] \oplus [-15., -10.1]$	$[-56., -46.3] \oplus [-5., 4.7]$	$[-36., -15.7]$
$\langle r^2_{\nu_\mu}\rangle$ (10^{-32}) cm^2	$[-54., -49.1] \oplus [-3., 2.1]$	$[-41., -37.8] \oplus [-14., -10.6]$	$[-55., -49.0] \oplus [-3., 3.4]$	$[-35., -31.2] \oplus [-20., -16.8]$
$\frac{\langle r^2_{\nu_e}\rangle}{\langle r^2_{\nu_\mu}\rangle_{\rm SM}} = \frac{\langle r^2_{\nu_e}\rangle}{\langle r^2_{\nu_\mu}\rangle_{\rm SM}}$	$1^{+2.9}_{-3.5}$	$1^{+3.0}_{-3.8}$	$1^{+3.2}_{-4.1}$	$1^{+4.0}_{-4.6}$
$R_n^{\rm pt}$ (fm)	$4.85^{+0.37}_{-0.39}$	$4.07^{+0.72}_{-0.83}$	$4.86^{+0.29}_{-0.35}$	< 4.24
μ_{ν_e} $(10^{-10}\mu_{\rm B})$	< 16	< 9.4	< 11	< 14
μ_{ν_μ} $(10^{-10}\mu_{\rm B})$	< 12	< 7.7	< 8.8	< 11
$g_Z'^{B-L}\big\vert_{M_{Z'}\lesssim 5\,\rm MeV}$	$< 1.4\times 10^{-5}$	$< 6.3\times 10^{-6}$	$< 7.1\times 10^{-6}$	$< 8.8\times 10^{-6}$
$\frac{g_{Z'}^{B-L}}{M_{Z'}/GeV}\Big\vert_{M_{Z'}\gtrsim 50\,\rm MeV}$	$< 4.9\times 10^{-4}$	$< 3.9\times 10^{-4}$	$< 3.5\times 10^{-4}$	$< 5.3\times 10^{-4}$

TABLE IV. Allowed ranges at 90% C.L. for the weak mixing angle (given as best fit $\pm 1.64\sigma$), neutrino charge radii for two flavour projections (and after marginalizing over the other), the point-neutron radius, the $\nu_{e,\mu}$ magnetic moments, and the model with a light vector mediator coupled to $B-L$ current (90% C.L. upper bound)

the sensitivity to this parameter for all detectors considered is comparable because it is mostly limited by the assumed 10% flux normalization uncertainty. To this end, we have explicitly verified that removing the QF uncertainty and/or the time information has no effect on these results. The ultimate 1σ statistics-limited sensitivity that could be achieved if there were no flux uncertainty is (1.3, 2.9, 1.2, 5.6) % at 1σ for the (CsI, Ge, Xe, Ar)-based detectors.

As mentioned above, the determination of the weak mixing angle is tightly related to the sensitivity to the effective flavour-dependent neutrino charge radius whose value in the SM (5.15) is

$$\langle r^2_{\nu_\alpha}\rangle = -\begin{pmatrix}0.83\\0.48\\0.3\end{pmatrix}\times 10^{-32}\,\text{cm}^2 \text{ for } \begin{pmatrix}\nu_e\\\nu_\mu\\\nu_\tau\end{pmatrix} \tag{5.22}$$

making the observation of this effect extremely challenging (see Ref. [142] for a recent review and compilation of bounds).

In BSM scenarios, the charge radii may receive additional contributions and, therefore, a measurement of their value well above the SM expectation would be a clear signal of BSM. In addition, in some BSM scenarios flavour transition charge radii $\langle r^2_{\alpha\neq\beta}\rangle$ can also be generated [61, 127]. For concreteness, we study the expected sensitivity for scenarios generating flavour-diagonal charge radii only.

Our results on the expected sensitivity for the flavour-diagonal charge radius are shown in Fig. 8 and Table IV. In the left panel of Fig. 8, we plot the 90% C.L. allowed regions in the plane $(\langle r^2_{\nu_e}\rangle, \langle r^2_{\nu_\mu}\rangle)$ for the four detectors under consideration. We list the corresponding 90% C.L. allowed ranges for each charge radius (after marginalizing over the other) in Table IV. As seen in the figure, for most detectors there are four distinct regions of which only one is centered at the SM predictions. The other three correspond to quasi-degenerate scenarios for which the charge radius is large enough to flip the sign of the SM $Q_{W,e}$ and/or $Q_{W,\mu}$ (CEνNS is sensitive to the *squared* weak charge). This happens when

$$\langle r^2_{\nu_{e,\mu}}\rangle \simeq -\frac{3}{m_W^2}\left(\frac{N-Z}{2Z\sin^2\theta_W}+2\right) . \tag{5.23}$$

For the Ar TPC, the limited time resolution and large backgrounds imply that the interaction of different flavours cannot be experimentally separated. Hence, data is not very sensitive to $Q^2_{W,e}$ and $Q^2_{W,\mu}$ separately, but to a combination instead (below we discuss this in more detail) and there is a continuous degenerate region where the combination has the same value as in the SM. The figure also illustrates the complementarity of the different targets and how combination of data taken with them (i.e., different N/Z) can help to break the 2×2 fold degeneracy and isolate a single region.

For comparison, in the curve labeled COHERENT we show the current constraints from the observation of CEνNS at the spallation source experiment COHERENT, as obtained in Ref. [118] by the combined analysis of results with CsI [141] and Ar [145] targets. Similar results were obtained in Refs. [143, 144] with a momentum-independent form factor (the assumption in our analysis). As seen from the figure, for all detectors under consideration JPARC is expected to improve over current bounds from the COHERENT CsI+Ar combination. The improvement is substantial for detectors with better time resolution (Cryogenic-CsI and HPGe), for which flavour discrimination is better; or detectors with moderate time resolution but negligible backgrounds (Xe TPC).

The role of the different sources of uncertainties is further illustrated in the right panel of Fig. 8, where we show the effect of the different uncertainties and time information in the final sensitivity (here for the Cryogenic-CsI detector as illustration, for other detectors the results

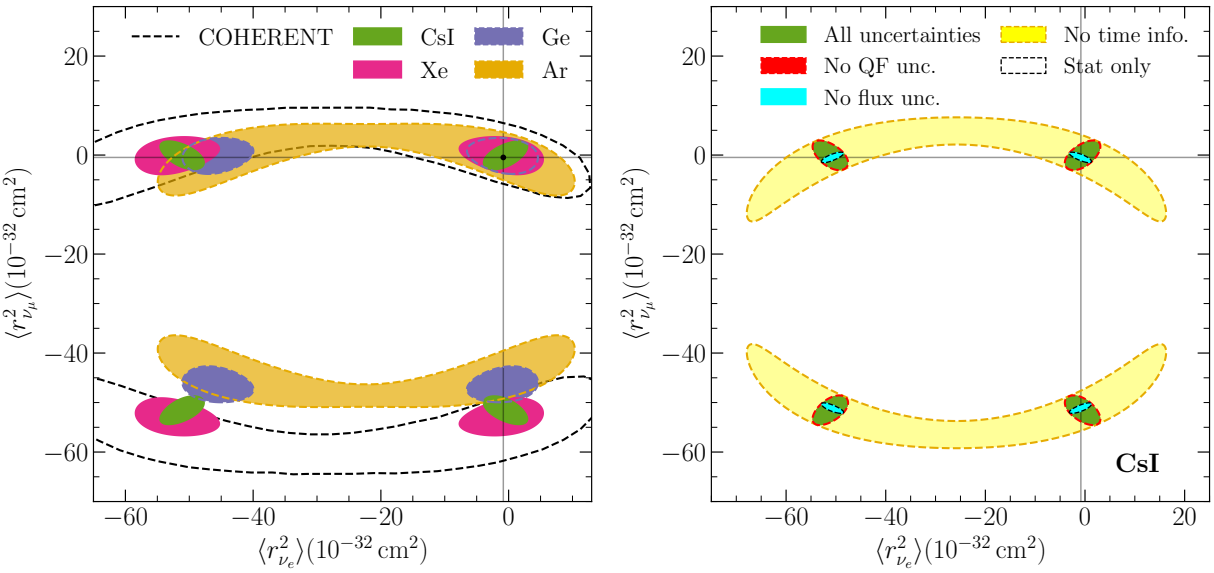

FIG. 8. Expected allowed regions in the $(\langle r^2_{\nu_e}\rangle, \langle r^2_{\nu_\mu}\rangle)$ plane at the 90% confidence level (C.L.) for two degrees of freedom (d.o.f.) ($\Delta\chi^2 = 4.61$) . **Left:** The different regions correspond to the expected results for the different detectors listed in Table II, as indicated by the legend. In all cases, the simulated data has been generated for the SM, and the results are then fitted assuming arbitrary values of the charge radii and including the nominal uncertainties and time resolution. For comparison we plot as the vertical and horizontal lines the SM predictions (Eq. (5.22)), and as dashed the current 90%CL bounds from the analysis of COHERENT CsI and Ar data from Ref. [118] (see also Refs. [143, 144]). **Right:** The allowed regions for the Cryogenic-CsI detector under different assumptions for the systematic uncertainties as labeled, see text for details.

are similar). The different regions are obtained removing one effect at a time. As seen in the figure, comparing the red contour and the green region, removing the QF uncertainty leads to very little effect, as the impact of the charge radius is energy-independent. Conversely, the results obtained removing only the flux uncertainty (cyan region) and removing all systematics (black dash contour) are practically equivalent. We conclude that the overall flux normalization is the dominant systematic error in this scenario. We have also verified that the systematic uncertainty on the intrinsic backgrounds has a very marginal effect on the results. This is expected given the smallness of the backgrounds (see Fig. 7). This result holds for all the physics scenarios we have studied.

We also illustrate the relevance of the time information by showing the allowed region (yellow) if we only bin in energy. In this case, the region becomes almost a ring. This is so because without time information the dominant effect is a global correction of the event rates in all energy bins. Requiring that the total number of events is compatible with the SM expectation, it is straightforward to show that (neglecting the small SM ν charge radius), the allowed confidence regions in the plane $(\langle r^2_{\nu_e}\rangle, \langle r^2_{\nu_\mu}\rangle)$ verify the equation of a circle

$$\left[R + \langle r^2_{\nu_e}\rangle\right]^2 + 2\left[R + \langle r^2_{\nu_\mu}\rangle\right]^2 = 3R^2 \tag{5.24}$$

where $R \equiv \frac{3}{m_W^2}\frac{N - Z(1-4\sin^2\theta_W)}{4Z\sin^2\theta_W}$. As seen in the figure, this full degeneracy is not exact. This is so because, as discussed in detail in Ref. [18], a detector with enough energy resolution, large statistics, and no saturation, has some residual flavour discrimination due to the different flavour composition of the beam above and below the maximum recoil allowed for the prompt ν_μ component. Nevertheless, the figure clearly illustrates the limited reach of this effect compared to the flavour-discriminating power of the timing information.

Finally, we note that the 2×2 fold degeneracy in Eq. (5.23) is absent in models in which the correction to the SM is flavour-independent. In this case, only values around the SM ones are allowed. Then, our results in Table IV show that the attainable precision at J-PARC MLF is comparable with the SM prediction. Indeed, the statistical uncertainty is small enough that without flux normalization uncertainties the SM value could be distinguished from 0. However, the flux uncertainty dominates the final result, making the overall uncertainty 3–4 times larger than the difference between the SM value and 0.

C. Neutron nuclear distribution radius

Since CEνNS is sensitive to the weak form factor, dominated by the coupling to neutrons, it can directly probe the distribution of neutrons in the nucleus. This provides complementary information to proton densities accessible with elastic electron scattering [132, 147]. At present the most precise direct measurement of a neutron distri-

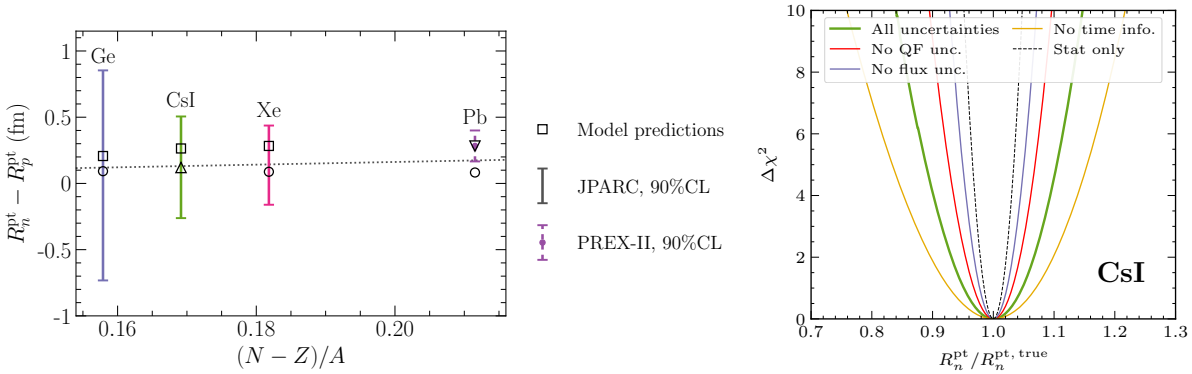

FIG. 9. **Left:** Compilation of our results for the expected sensitivity of the neutron skin thickness $R_n^{\rm pt} - R_p^{\rm pt}$ with 90% C.L., one d.o.f, ($\pm 1.64\sigma$) for the different detectors as labeled in the figure. For comparison we show the result for ^{208}Pb derived from the PREX measurement with the analysis in Ref. [146] and the best-fit to the indirect determination from antiprotonic atom x-ray data for a variety of nuclei (dashed line), taken from Ref. [134]. The hollow markers represent the range of predictions from different nuclear models. **Right:** $\Delta\chi^2$ as a function of $R_n^{\rm pt}({\rm CsI})/R^{\rm pt,true}({\rm CsI})$ under different assumptions for the systematic uncertainties as labeled, see text for details.

bution comes from parity-violating electron scattering in ^{208}Pb [148, 149], also sensitive to the weak form factor. Alternative measurements rely on nuclear [134, 150–153] or electromagnetic [154] reactions which probe both neutron and proton distributions, but they lean on model-dependent analyses (with uncertainties that are difficult to quantify). Likewise, atomic parity violation experiments are also sensitive to the nuclear neutron distribution, but they are subject to model-dependent uncertainties from atomic many-body calculations.

Given the low momentum transfers involved in CEνNS, the form factors can be characterized using the first moment of the weak charge distribution in Q^2, R_W in Eq. (5.18)), or what is the same, in terms of the point-proton $R_p^{\rm pt}$ and point-neutron distribution radii $R_n^{\rm pt}$. In the last years, different phenomenological analysis of the data from CEνNS observations have provided determinations of the neutron distribution radius on CsI [60, 61, 64, 66, 68, 69, 91, 98], Ar [62, 103], and Ge [65] with consistent results such as

$$\begin{aligned} R_n({\rm CsI}) &= 5.47^{+0.63}_{-0.72}\ {\rm fm}\ (90\%\,{\rm C.L.})\ [64] \\ R_n({\rm Ar}) &\leq 6.2\ {\rm fm}\ (2\sigma\,{\rm C.L.})\ [62] \\ R_n({\rm Ge}) &= 6.5 \pm 3\ {\rm fm}\ (2\sigma\,{\rm C.L.})\ [65] \end{aligned} \tag{5.25}$$

Our results on the expected sensitivity for the point-neutron radius are shown in Fig. 9 and Table IV. In the table we show the expectations for the 95% C.L. allowed range for each of the considered targets with the central value corresponding to the true value of the weighted averaged over the considered isotopes (see table III). These predictions clearly represent a substantial improvement over our current knowledge. On that end, we plot in the left panel in Fig. 9 our results in the form of the expected sensitivity of the neutron skin thickness $R_n^{\rm pt} - R_p^{\rm pt}$ as a function of $(N-Z)/(N+Z)$. For comparison, Fig. 9 shows the neutron skin thickness for ^{208}Pb, derived from the analysis in Ref. [146] of the results of the Lead Radius Experiment (PREX) experiment [148, 149] on parity-violation in electron scattering which, as mentioned above contains certain model dependence. In this figure we also show the best-fit for the neutron skin obtained from its indirect determination from antiprotonic X-ray data for a variety of nuclei (dashed line), taken from Ref. [134]. Finally, the hollow markers show the predictions for a variety of nuclear models [155–157].

The results also show that, unlike for the Weinberg angle, the attainable precision for the point-neutron radius is worse for Ge (and much worse for Ar) than for Xe or CsI. This is expected on the basis of statistics, because the signal statistics grows quadratically with the number of neutrons in the target nucleus. Besides that, the lighter the nucleus the smaller the values of $R_{p,n}^{\rm pt}$ (or, equivalently, R_W), and the weaker the dependence of the form factor with Q^2, reducing the energy dependence of the effect and making it more difficult to disentangle from the overall normalization uncertainty. To illustrate the relevance of the different systematic uncertainties on the attainable sensitivity we plot in the right panel (Figure 9) the dependence of $\Delta\chi^2$ on $R_n^{\rm pt}({\rm CsI})$ for different assumptions on the systematic uncertainties. First we notice that, while the flux normalization keeps being the main systematic uncertainty, the assumed precision on the QF plays also an important role. This is so because the effect of $R_n^{\rm pt}$ is to suppress the number of events at large recoil energies as coherence gets lost. The energies at which this suppression happens are directly related with the value of $R_n^{\rm pt}$, and a QF uncertainty is equivalent to an uncertainty in the reconstructed nuclear recoil energy, i.e., an uncertainty in the reconstructed $R_n^{\rm pt}$. Finally we also observe that despite the effect being flavour-independent, there is a certain loss of sensitivity if the time information is not included. This is due to the different energy dependence of the events from the prompt and delayed

neutrinos. Thus, timing information aids in establishing the T-dependence of the effect.

Overall, we find that statistical and systematic effects are comparable in this measurement. As an illustration, if the CsI detector mass were increased up to 1 tonne (assuming that backgrounds scale up proportionally), we find that the 90% C.L. uncertainty on the point neutron radius would decrease by a factor ~ 4.

D. Non-standard neutrino interactions

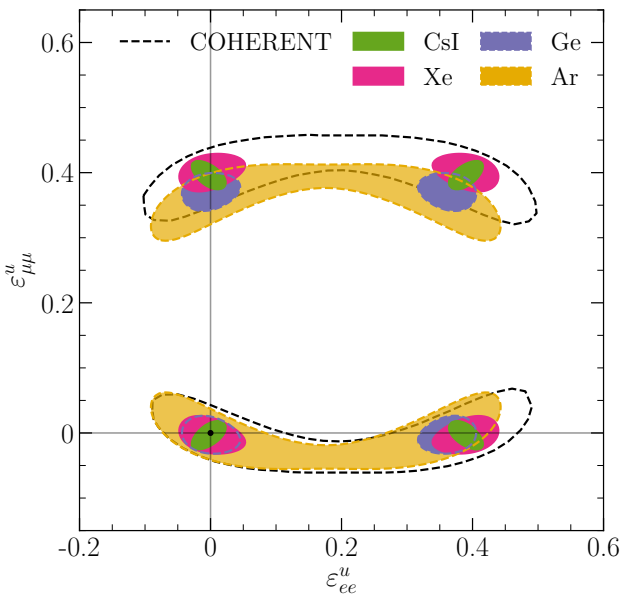

FIG. 10. Expected allowed regions in the $(\epsilon^{u,V}_{ee}, \epsilon^{u,V}_{\mu\mu})$ plane at the 90% confidence level (C.L.) for two d.o.f. ($\Delta\chi^2 = 4.61$). The different regions correspond to the expected results for the different detectors listed in Table II, as indicated by the legend. For simplicity, the rest of the NSI parameters not shown in the figure have been assumed to be zero. In all cases, the simulated data has been generated for the SM, and the results are then fitted assuming arbitrary values of the two NSI coefficients and including the nominal uncertainties and time resolution. The dashed contour shows the current 90% CL bounds from the analysis of COHERENT CsI and Ar data from Ref. [118].

From a completely model-independent approach, a useful parametrization of the possible BSM effects at low energies is through the addition of higher-dimensional operators to the SM Lagrangian. At dimension 6, the allowed set of operators includes four-fermion operators affecting neutrino production, propagation, and detection processes. These are the so-called non-standard neutrino interactions (NSI). For example, the effective Lagrangian

$$\mathcal{L}^{\rm NC}_{\rm NSI} = -\sum_{f,\alpha,\beta} 2\sqrt{2}\, G_F\, \varepsilon^{f,P}_{\alpha\beta}\, (\bar{\nu}_\alpha \gamma_\mu P_L \nu_\beta)\, (\bar{f}\gamma^\mu P f) \ , \quad (5.26)$$

would lead to new NC interactions with the rest of the SM fermions. Here, $\alpha, \beta \equiv e, \mu, \tau$ while f refers to SM fermions, and P can be either a left-handed or a right-handed projection operator (P_L or P_R, respectively). Such new interactions may induce lepton flavour-changing processes (if $\alpha \neq \beta$), or may lead to a modified interaction rate with respect to the SM result (if $\alpha = \beta$).

As for their effect in CEνNS, in presence of NC NSI, the CEνNS cross section can still be written as Eq. (5.11) with and effective charge of the nucleus Eq. (5.12), $\mathcal{Q}^2_{W,\alpha} \to \mathcal{Q}^2_\alpha(\varepsilon)$. For real NSI parameters, it can be written as [70]

$$\mathcal{Q}^2_\alpha(\varepsilon) = \left[\mathcal{Q}_{W,\alpha} + 2\,\varepsilon^{\rm X}_{\alpha\alpha}\right]^2 + 4\sum_{\beta\neq\alpha} \left(\varepsilon^{\rm X}_{\alpha\beta}\right)^2 \ , \quad (5.27)$$

with

$$\varepsilon^{\rm X}_{\alpha\beta} \equiv (N+2Z)\varepsilon^{u,V}_{\alpha\beta} + (2N+Z)\varepsilon^{d,V}_{\alpha\beta} \quad (5.28)$$

being the effective nuclear NSI vector couplings in terms of those of the quarks, $\varepsilon^{q,V}_{\alpha\beta} \equiv \varepsilon^{q,L}_{\alpha\beta} + \varepsilon^{q,R}_{\alpha\beta}$. Thus, the first consequence we observe of including NSI effects is that the weak charge may now strongly depend on the incident neutrino flavour α.

At present, the best constraints available in the literature for these operators come from global fits to oscillation data, which are very sensitive to modifications in the effective matter potential felt by neutrinos as they propagate in a medium [158]. Consequently, they can strongly bound vector NSI, and, since they are due to a totally coherent effect, these bounds extend to NSI induced even by ultra light mediators ($M_{\rm med} \gtrsim 1/R_{\rm Earth} \sim \mathcal{O}(10^{-12})\,$eV). However, while oscillation experiments are sensitive to all flavour-changing NSI, they are only sensitive to differences between the diagonal NSI parameters in flavour space [76, 158]. This leads to the appearance of new degeneracies involving standard oscillation parameters and NSI operators, such as the so-called LMA-DARK/generalized mass ordering degeneracy [159–161]. Conversely, as seen above, CEνNS experiments at spallation sources allow to constrain two of the three flavour-diagonal coefficients, lifting the degeneracy and allowing for the independent determination of all the NSI with the combined analysis of oscillation and CEνNS [87, 158, 162].

With this in mind, in what follows we focus on the determination of the flavour-diagonal NSI coefficients, $\epsilon^{f,V}_{\alpha\alpha}$ ($f = u, d$), although it should be kept in mind that coherent neutrino scattering is also sensitive to all the off-diagonal NSI operators as well, and competitive sensitivity should also be expected for those.

Our results on the expected sensitivity for the NSI coefficients are shown Fig. 10. There we plot the 90% C.L. allowed regions in the plane $(\epsilon^{u,V}_{ee}, \epsilon^{u,V}_{\mu\mu})$ for different detector materials (left panel). In this figure, for simplicity, we have assumed that the NSI take place only with up-type quarks; however, similar results are obtained if the

NSI are assumed to take place with down-type quarks instead.

Non-surprisingly, comparing Fig. 10 and Fig. 8 we observe that the main qualitative features are very similar. In brief, the allowed region consists of four distinct sections because $\mathcal{Q}_e^2$ and $\mathcal{Q}_\mu^2$ can be independently determined from timing information. This results in two allowed ranges for each of the NSI coefficients considered. One of the four regions is centered at the SM prediction, ($\epsilon_{ee}^{u,V} = \epsilon_{\mu\mu}^{u,V} = 0$); the other three correspond to the quasi degenerated solutions which in this case happen when $\varepsilon_{\alpha\alpha}^X = -\mathcal{Q}_{W,\alpha}$, i.e $\varepsilon_{\alpha\alpha}^{u,V} \simeq \frac{N-Z(1-4\sin^2\theta_W)}{N+2Z}$. As in Fig. 8, for the Ar TPC, limited time resolution and large backgrounds hinder a separate measurement of $\mathcal{Q}_e^2$ and $\mathcal{Q}_\mu^2$. It is also clear from the figure that, because the impact of NSI on the weak charge depends on the values of N and Z in a non-trivial manner, the combination of data obtained for different nuclei offers an additional handle to reduce the size of the allowed confidence regions of this scenario (for earlier discussions see, e.g., Refs. [18, 70, 76, 163]).

In the figure we also show for comparison the current constraints from COHERENT, as obtained in Ref. [118] by the combined analysis of results with CsI [141] and Ar [145] targets. The figure clearly illustrates the improved sensitivity due to the flavour discrimination induced by the precise time-structure information of the neutrino signal stemming form the pulsed nature of the J-PARC proton beam, together with the significantly improved statistics.

We find that the effect of the different systematics and time information is also very similar to that shown in the right panel of Fig. 8, i.e., the dominant source of systematic uncertainty is the overall flux normalization. And most importantly, as discussed above, in absence of time information, the experiments are mostly sensitive to the combination $\mathcal{Q}_e^2 + 2\,\mathcal{Q}_\mu^2$. This would result in a ring-like allowed region around $(R+\epsilon_{ee}^{u,V})^2 + 2(R+\epsilon_{\mu\mu}^{u,V})^2 = 3R^2$ where now $R \equiv \frac{-N+Z(1-\sin^2\theta_W)}{2(2Z+N)}$. In this case, the only flavour information comes from the marginal variation of the flavour composition with recoil energy.

As for the neutron radius measurement, the determination of NSI is not only statistics-limited. As an illustration, if the CsI detector mass were increased up to 1 tonne (assuming that backgrounds scale up proportionally), we find that the major axis of each allowed ellipse in Fig. 10 would not change, as it is dominated by flux uncertainties (see Fig. 8 right). The minor axis would, however, shrink by a significant factor.

E. Light vector mediators

$U(1)$ extensions of the SM gauge symmetry are one of the most minimal forms of BSM physics. They appear in many top-down models which contain a heavy ($\sim$ TeV scale) neutral gauge boson (Z') [164]. More recently, $U(1)$ extensions where new gauge boson is light have been widely studied, in particular in scenarios able to provide novel Dark Matter candidates [165].

From the point of view of their effect in CEνNS, these extensions can be described in terms of the Lagrangian for the interaction of the neutral vector Z' with the fermions participating in the process:

$$\mathcal{L}_{Z'} = g_{Z'} Z'_\mu \sum_{\substack{f=u,d,e,\\ \nu_{eL},\nu_{\mu L}}} q_{Z'}^f \left(\bar{f}\gamma^\mu f\right) + \frac{1}{2} M_{Z'}^2 Z'^\mu Z'_\mu \,, \quad (5.29)$$

where $q_{Z'}^f$ indicates the charge of each fermion f under the new $U(1)$ interaction.

The amplitude for neutrino scattering off nuclei mediated by the Z' interferes with that of the SM, so the additional contribution to the neutrino-nucleus scattering cross section reads [74]

$$\Delta\frac{d\sigma_{Z',\alpha}}{dT} = \frac{g_{Z'}^2 M}{2\,\pi}\left[\frac{g_{Z'}^2 (q_{Z'}^\nu)^2 \mathcal{Q}_{Z'}^2}{(2MT+M_{Z'}^2)^2} - \frac{\sqrt{2}G_F q_{Z'}^{\nu_\alpha}\mathcal{Q}_{Z'}\mathcal{Q}_W}{(2MT+M_{Z'}^2)}\right] \times \left(1-\frac{MT}{2E_\nu^2}\right)|F(Q)|^2 \,, \quad (5.30)$$

where $\mathcal{Q}_{Z'}$ is the weak charge of the nucleus for the light vector interaction and $F(Q^2)$ is the form factor that, with enough precision at the momentum transfers of interest, can be assumed to be the same as in the SM [157]. Vector current conservation implies that only valence quarks contribute by simply summing up their charges, so for universal couplings ($q_{Z'}^u = q_{Z'}^d \equiv q_{Z'}^q$), $\mathcal{Q}_{Z'} = 3\,q_{Z'}^q\,(Z+N)$ (see, e.g., Ref. [166]).

With existing CEνNS data, limits on a variety of vector boson mediator models have been derived (see e.g. Refs. [80, 81, 84, 86, 97–99, 102, 106, 118, 119, 143, 167, 168] for an incomplete list).

For the sake of concreteness we show our results of the expected sensitivity for a Z' coupling to $B-L$ (for which $-1 = q_{Z'}^{\nu_e=} = q_{Z'}^{\nu_\mu} = -3q_{Z'}^u = -3q_{Z'}^d$). This is an anomaly-free model which represents an example of a fully consistent UV completion for the NSI phenomenological parametrization. The results are shown in Fig. 11, where in the left panel we plot the expected excluded regions in the $(g_{Z'}^{B-L}, M_{Z'})$ plane at the 90% C.L. with the detectors under consideration. For light mediator masses ($M_{Z'} \lesssim$ 5–10 MeV depending on the detector threshold), the experiment has no sensitivity to the mediator mass and the limit of the regions approaches a horizontal line of constant coupling. For these effectively massless scalar mediators, it is possible to derive an upper bound on the coupling constant independent of mediator mass, which we list in Table IV. Conversely, for sufficiently large mediator masses, the boundary is a diagonal, characteristic of the contact-interaction limit. In that case, the event rates depend on $(g_{Z'}/M_{Z'})^2$. This is the limit in which

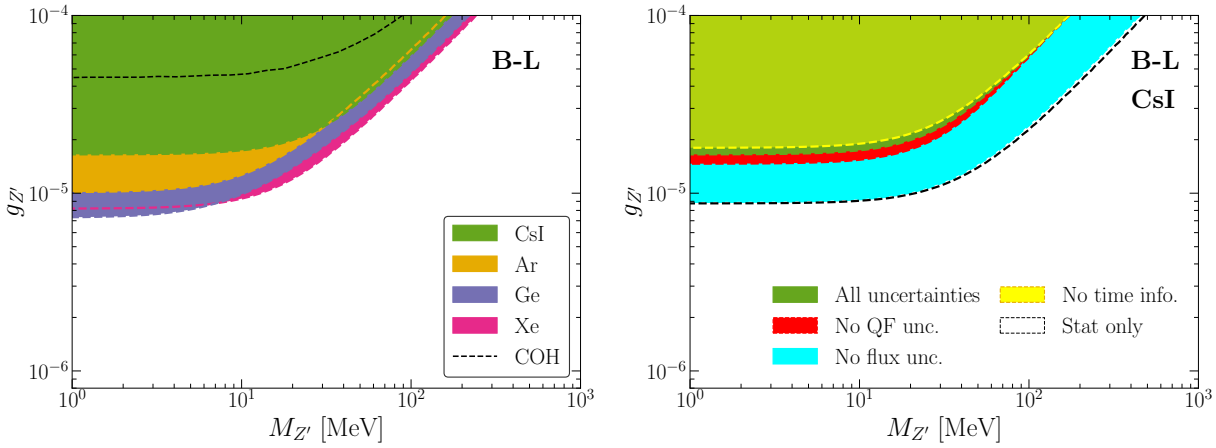

FIG. 11. Expected excluded regions in the $(g_{Z'}^{B-L}, M_{Z'})$ plane at the 90% confidence level (C.L.) for two d.o.f. ($\Delta\chi^2 = 4.61$). **Left:** The different regions correspond to the expected results for the different detectors listed in Table II, as indicated by the legend. In all cases, the simulated data has been generated for the SM, and the results are then fitted assuming arbitrary values of the Z' coupling and mass and including the nominal uncertainties and time resolution. The dashed line shows the current 90% CL bounds from the analysis of COHERENT CsI and Ar data from Ref. [118]. **Right:** The excluded regions for the Cryogenic-CsI detector under different assumptions for the systematic uncertainties as labeled, see text for details.

the effect can be described via an NSI parametrization

$$\varepsilon_{\alpha\alpha}^{u,B-L} = \varepsilon_{\alpha\alpha}^{d,B-L} = \frac{1}{3\sqrt{2}G_F}\frac{g_{Z'}^2}{M_Z'^2} \tag{5.31}$$

We list in Table IV the bounds on $\frac{g_{Z'}^2}{M_Z'^2}$ in this regime.

For comparison, in the curve labeled COH, we show the current constraints from COHERENT, as obtained in Ref. [118] by the combined analysis of results with CsI [141] and Ar [145] targets. (Consistent results but with a different CL were obtained in Ref. [167].) As seen in the figure, for all detectors considered, one foresees an improvement with respect to current bounds from COHERENT. For example, the reach on $g_{Z'}$ can improve by a factor $\sim$ 3–5 in the light-mediator mass regime. Light-mediator models are constrained by a plethora of laboratory experiments and well as cosmological observations. Comparing with the latest compilation in Fig. 5 in Ref. [167], for the $B-L$ model CEνES bounds provide the strongest constraints in the mass window $50\,\text{MeV} \lesssim M_{Z'} \lesssim 500\,\text{MeV}$.

The role of the different sources of uncertainty in this scenario is shown in the right panel of Fig. 11 (for the Cryogenic-CsI detector as illustration). As seen in the figure, comparing the red contour and the green region, removing the QF uncertainty has a marginal effect that is most relevant at low mediator masses, where the experiment threshold sets the sensitivity. We also see that, for this model, the timing information has very small impact. This is expected, as it is a lepton-flavour universal model. In this case, the dominant uncertainty is the overall flux normalization. As seen in the figure, reducing it can lead to an improvement of the sensitivity by a factor ~ 2.

Finally, let us notice that in deriving the sensitivity to this scenario we have only considered the effect of scattering off the nucleus, and we have not included the possible effect of scattering off electrons in the target. Therefore, our sensitivity can be considered to be conservative.

F. Neutrino magnetic moment

The neutrino magnetic moment is the electromagnetic neutrino property most experimentally searched for, as it is predicted to be non-zero for massive neutrinos with non-negligible values in a wide spectrum of BSM neutrino mass models. Laboratory and solar neutrino experiments (among others) bound the ν_e (ν_μ) magnetic moments at the level of 10^{-11} μ_B (10^{-9} μ_B) [133, 142].

In the presence of a neutrino magnetic moment, μ_ν, the cross section for neutrino scattering off nuclei gets additional contributions, which do not interfere with the SM ones. The scattering off protons can be considered coherent and therefore its cross section is given, up to order $\mathcal{O}(T/E_\nu)^2, (T/M)$, by [126]

$$\frac{d\sigma_{\mu_\nu}}{dT} = Z^2 \left(\frac{\mu_\nu}{\mu_B}\right)^2 \frac{\alpha^2\,\pi}{m_e^2}\left[\frac{1}{T} - \frac{1}{E_\nu}\right] |F_{\rm em}(Q^2)|^2 \,. \tag{5.32}$$

Since the effect due to a non-zero magnetic moment is only relevant for very low recoils, the electromagnetic form factor $F_{em}(Q^2)$ can be safely approximated to one. Notice also that, in writing Eq. (5.32), we have denoted the neutrino magnetic moment as μ_ν, without specifying the neutrino flavour. However, neutrino magnetic moments arise in a variety of models of new physics and, in particular, they do not need to be flavour-universal.

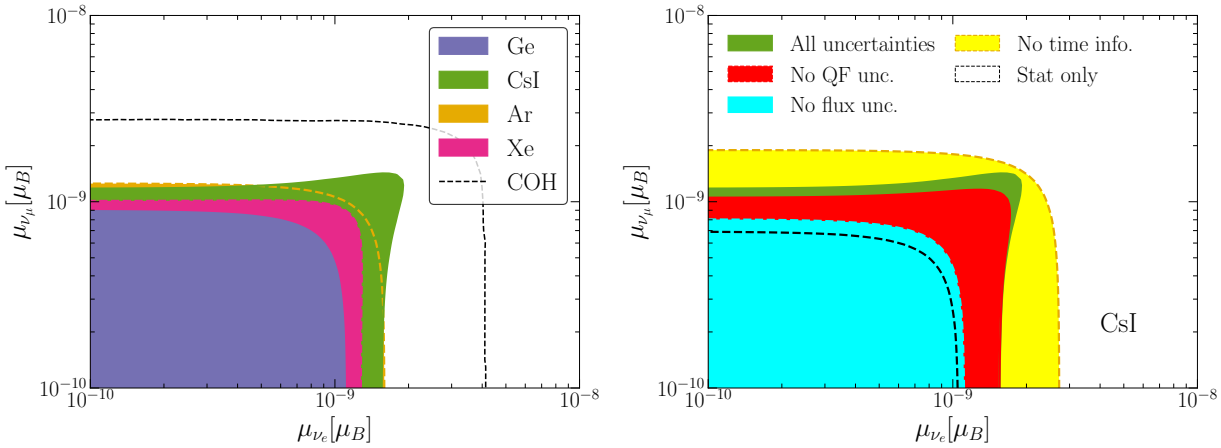

FIG. 12. Expected allowed regions in the $(\mu_{\nu_e}, \mu_{\nu_\mu})$ plane at the 90% confidence level (C.L.) for two d.o.f. ($\Delta\chi^2 = 4.61$). **Left:** The different regions correspond to the expected results for the different detectors listed in Table II, as indicated by the legend. In all cases, the simulated data has been generated for the SM, and the results are then fitted assuming arbitrary values of the two magnetic moments coefficients and including the nominal uncertainties and time resolution. The dashed line shows the current 90% CL bounds from the analysis of COHERENT CsI and Ar data from Ref. [118]. **Right:** The excluded regions for the Cryogenic-CsI detector under different assumptions for the systematic uncertainties as labeled, see text for details.

Therefore, in what follows, we allow different magnetic moments for the different neutrino flavours, reporting the sensitivity separately.

Our results on the expected sensitivity to neutrino magnetic moments with the detectors under consideration are shown in Fig. 12 and summarized in Table IV. From these expectations, we see that the relative performance of the different detectors is different than in the previous scenarios considered. In particular, we see that the Ar TPC sensitivity is comparable to that of the CsI detector. This is so because the effect of a finite neutrino magnetic moment on the CEνNS event rates is most noticeable for small recoil energies (below $0.5-1$ keV$_{nr}$ for $\mu_{\nu_\mu} \sim 10^{-10}\,\mu_B$). Therefore, it is expected that detectors with the lowest possible recoil energy threshold will be more sensitive to this neutrino property. Furthermore, the relative effect of the new contribution compared to the SM grows with $\sim (Z/N)^2$ which is ~ 0.65 for Ar and Ge and ~ 0.5 for Xe and CsI. Altogether, we find that the Xe TPC and HPGe PPC detectors provide the best sensitivity with a slightly better performance of the HPGe PPC driven mostly by its lower threshold.

For comparison, we also show in the left panel the current constraints from COHERENT, as obtained in Ref. [118] by the combined analysis of results with CsI [141] and Ar [145] targets. Equivalently, the quoted one-dimensional bounds read $\mu_{\nu_e(\nu_\mu)} < 38(26)\times10^{-10}\,\mu_B$ at 90% CL, which compared with the corresponding values quoted in Table IV show an improvement of up to a factor $\mathcal{O}(3.5)$. For μ_{ν_μ} these bounds are competitive with constraints from other laboratory experiments, but they are always much weaker than those obtained from solar neutrinos in Borexino [169, 170] and in direct Dark Matter detection experiments (see the comprehensive compilation in Ref. [142]).

The role of the different sources of uncertainty and of the time information in this scenario is further illustrated in the right panel of Fig. 12 (for the case of Cryogenic-CsI detector as an example). As we see, different uncertainties have a comparable impact, with flux uncertainty being the most relevant. Time information is also relevant, particularly when the magnetic moment is flavor-dependent.

G. Light sterile neutrinos

Historically, models with extended light neutrino sectors were invoked to explain a set of anomalies observed at short baselines that could not be explained within the standard 3ν framework. These anomalies could be interpreted as hints for the existence of additional neutrino states with masses at the eV scale. This requires the introduction of sterile neutrinos, i.e., SM singlets that mix with the three standard neutrinos, generating flavour oscillations at shorter distances.

At the baselines $\mathcal{O}(m)$ considered for CEνNS, the dominant effect of such oscillations is the depletion of active neutrino fluxes arriving to the detector. As CEνNS is sensitive to all neutrino flavors with the same SM interactions, it can directly test this depletion. Thus, it has been studied to provide constraints on this scenario, which can be relevant for the interpretation of the SBL anomalies [92, 105, 176].

Focusing on the 3+1 scenario, the expected number of events can be obtained as described in Sec. V A (neglecting the effect of the neutrino charge radius), where now

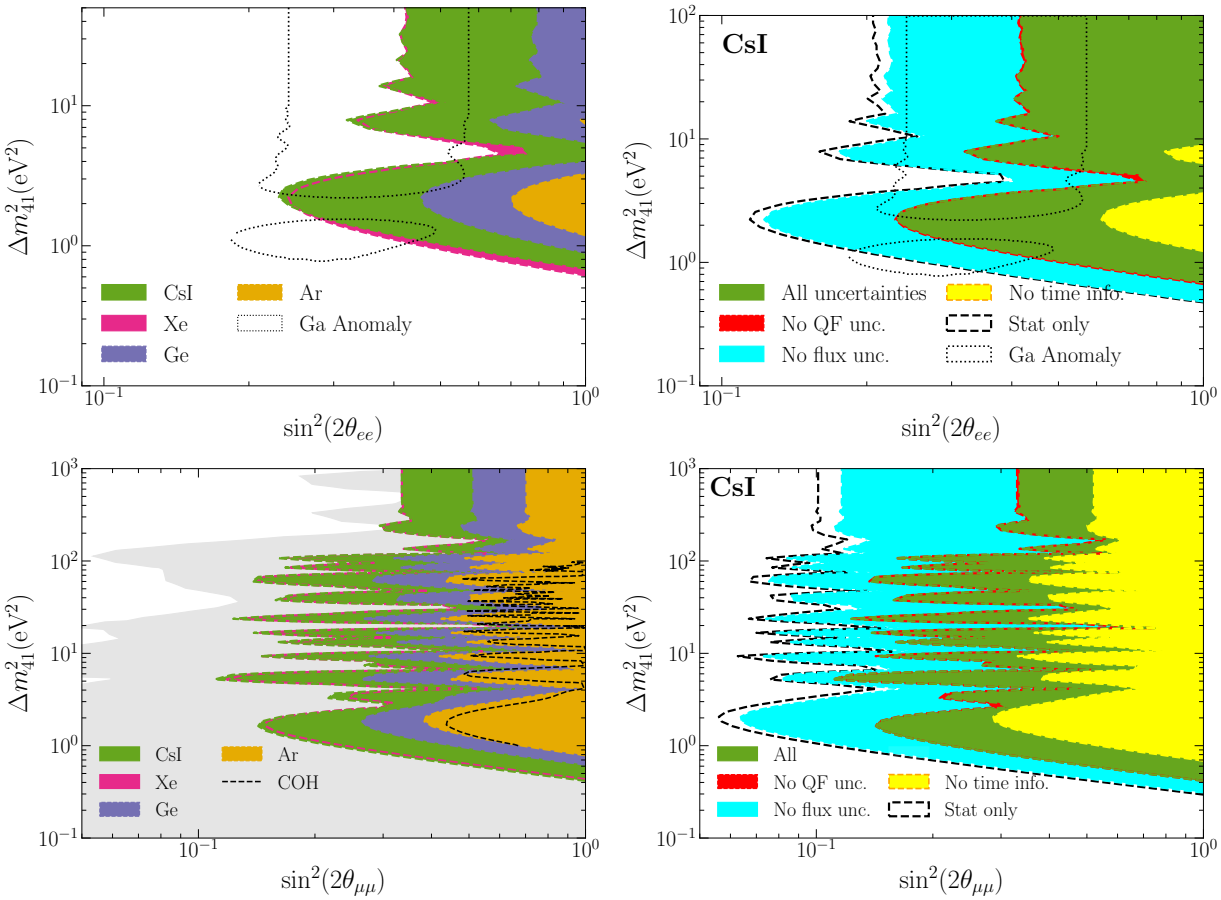

FIG. 13. Expected excluded regions in the $(\sin^2 2\theta_{ee(\mu\mu)}, \Delta m^2_{41})$ plane at the 90% confidence level (C.L.) for two d.o.f. ($\Delta\chi^2 = 4.61$). **Left:** The different regions correspond to the expected results for the different detectors listed in Table II, as indicated by the legend. In all cases, the simulated data has been generated for the SM, and the results are then fitted assuming arbitrary values of the two oscillation parameters and including the nominal uncertainties and time resolution. **Right:** The excluded regions for the Cryogenic-CsI detector under different assumptions for the systematic uncertainties as labeled, see text for details. In the upper plots for comparison we also show the 2σ region of the parameters which could explain the Gallium anomaly (from Ref. [171]). In the lower left plot we show the bounds from the analysis of COHERENT CsI and Ar data from Ref. [118] (dashed lines), and the envelope of current limits from the most constraining experiments in this mass range [172–175] (shaded grey region).

the energy dependent function is

$$g_X(T) \propto \int_{E_\nu^{\min}}^{\infty} dE_\nu \, P_{Xa}(E_\nu)\, \phi_X(E_\nu) \frac{d\sigma_X}{dT}(E_\nu, T)\,, \quad (5.33)$$

with the probabilities of neutrinos of flavour $X = \{e, \mu\}$ converting into *any* active neutrino given by

$$P_{Xa}(E_\nu) = 1 - 4|U_{X4}|^2(1 - \sum_{\alpha=e,\mu,\tau} |U_{\alpha 4}|^2) \sin^2\left(\frac{\Delta m^2_{41}}{2E_\nu}\right)\,. \quad (5.34)$$

For concreteness, we consider two cases. In the first case we will assume $U_{\mu 4} = U_{\tau 4} = 0$, for which $P_{\mu a}$=1 and

$$P_{ea} = 1 - \sin^2 2\theta_{ee} \sin^2\left(\frac{\Delta m^2_{41}}{2E_\nu}\right) \quad (5.35)$$

with $\sin^2\theta_{ee} \equiv |U_{e4}|^2$. This is the scenario invoked as possible explanation for the so-called Gallium anomaly [171, 177]. In brief, the radioactive source experiments at the Gallium solar neutrino experiments both in SAGE and GALLEX/GNO obtained an event rate lower than expected. This result was confirmed by the BEST experiment [171]. The effect can be explained by the hypothesis of ν_e disappearance due to oscillations with $\Delta m^2 \gtrsim 1$ eV^2 [177]. This interpretation, however is in tension with the analysis of solar neutrino experiments [178], and with latest KATRIN results [179]. Interestingly, CEνNS can directly test the hypothesis of neutrinos converting into a flavour without SM neutral current interactions, with less dependence on the underlying mechanism.

In the second case we assume $U_{e4} = U_{\tau 4} = 0$, for which

P_{ea}=1 and

$$P_{\mu a} = 1 - \sin^2 2\theta_{\mu\mu} \sin^2 \left(\frac{\Delta m^2_{41}}{2E_\nu} \right) \tag{5.36}$$

with $\sin^2 \theta_{\mu\mu} \equiv |U_{\mu 4}|^2$.

We plot in Fig. 13 the regions of oscillation parameters which can be excluded at the 90% C.L. with the detectors under consideration. In the upper panels we show the results for the $U_{\mu 4} = U_{\tau 4} = 0$ case. For sake of comparison, we also show the 2σ parameter region which could explain the anomaly [171]. As seen in the figure, the best sensitivity for this scenario is attainable with the Cryogenic-CsI and the Xe TPC detectors which can probe part of the parameter space required to explain the anomaly, though they are not competitive with the bounds from solar experiments and KATRIN.. In the right panel, we show the impact of the different uncertainties and of the time information in this scenario on this conclusion. As seen in the figure, the dominant uncertainty is that of the overall flux normalization, which is expected since the effect of the oscillation into sterile neutrinos is in this case the depletion of the ν_e flux. Since ν_μs are not affected, the sensitivity is strongly dependent on flavour discrimination, hence the relevance of the timing information observed in the right panel of the figure.

Conversely, the lower panels show the results for the $U_{e4} = U_{\tau 4} = 0$ case. Because of the monochromatic nature of prompt ν_μ, the oscillatory behaviour of the survival probability does not get averaged by the experimental energy resolution. In this case, we consider the effect of the smearing over the uncertainty in the baseline, which for an $\mathcal{O}(\%)$ uncertainty results into averaged oscillations for $\Delta m^2_{41} \sim \mathcal{O}(\text{few } 10^2)$ eV^2. In our analysis, we adopt a 0.5% baseline uncertainty for all targets. We have verified that varying this uncertainty from 1 cm to 30 cm does not affect the exclusion contour at low masses ($\Delta m^2_{41} \lesssim 100$ eV^2), and it only slightly modifies the amplitude of the last two oscillation peaks before averaging it out.

For this channel, we can also compare with the sensitivity obtained with the analysis of COHERENT CsI and Ar data in Ref. [118], over which we find that all detectors can provide an improvement. We also compare with the present exclusion from the most constraining experiments in this mass range [172–175] shown as the shaded grey region in the figure. As seen in the figure, some of the detectors in consideration hold the potential to yield dominant sensitivity for $\Delta m^2_{41} \sim (2\text{–}4) \times 10^2$ eV^2 provided the aforementioned uncertainty on the baseline can be guaranteed. Finally, from the right panels we see that the relative behaviour of the different detectors and the relevance of the impact of the different uncertainties is similar for both oscillation channels.

VI. CONCLUSIONS

In this work we have explored the prospects of J-PARC MLF for CEνNS studies. In order to quantitatively assess the potential of our proposal, we have explored the sensitivity to a broad spectrum of SM effects —including the weak mixing angle, the neutrino charge radii and the neutron nuclear radius — and BSM scenarios, such as NSI, new light mediators, neutrino magnetic moments, and $\mathcal{O}$(eV) sterile neutrinos. We have considered as examples a variety of detector technologies presently funded for construction and under development, with different nuclear targets (listed in Table II). In our studies, we have taken into account the careful characterization and evaluation of the expected background sources and their energy and time dependence, as described in Sec. III.

We have also analyzed the relative effect of the main sources of systematic uncertainties: the overall flux normalization, the QF uncertainty, and the uncertainty on the normalization of the irreducible backgrounds. Our results show that for all scenarios and detector technologies considered, the overall flux normalization is the dominant systematic uncertainty. Any improvement on this uncertainty would largely enhance the sensitivity of the expected vast statistics (see, e.g., Fig. 7).

We also find that for flavour-independent effects, such as variations of the weak mixing angle, or scenarios with new universal interactions, all technologies deliver comparable sensitivity. Differences are only determined by the statistics attainable in the different detectors, and/or the nuclear charge dependence of the scenario (see Table IV and Fig. 11). Conversely, larger differences in the performance are found for flavour-dependent effects (in particular for charge radii, NSI, and sterile neutrinos). For them, including the precise time-structure information of the neutrino signal stemming form the pulsed nature of the J-PARC proton beam substantially boosts the sensitivity for detectors with good time resolution (see Figs. 8 and 13). A notable exception to this general behavior is the neutrino magnetic moment, for which the reach of a given detector also depends strongly on its recoil energy threshold. All in all, our results illustrate the well–known boost in sensitivity attainable by employing a variety of detectors with different nuclear targets. For all scenarios studied we have showed the improvement in sensitivity compared with current constraints from the from the observation of CEνNS at the spallation source experiment COHERENT. In particular, we find that the expected sensitivity can result in leading bounds on neutrino charge radius, neutron nuclear distribution radius, laboratory constraints on NC-NSI, interactions with light mediators in the mass window $\mathcal{O}$(100 MeV), and potentially ν_μ-sterile oscillations with $\Delta m^2 \sim \mathcal{O}(\text{few } \times 10^{-2}\,\text{eV}^2)$.

The J-PARC proton beam already serves important neutrino experiments including Super-Kamiokande and JSNS^2. As we have shown, CEνNS measurements are not

only feasible at this facility, but they would provide leading statistics and excellent physics sensitivity. As such, they would complement the physics program of Hyper-Kamiokande, for example, by breaking well-known degeneracies between standard oscillation and some New Physics effects in long baseline neutrino oscillation experiments. Altogether, CEνNS activities would significantly boost the neutrino-physics output of J-PARC MLF, with relatively low effort.

ACKNOWLEDGMENTS

This work is funded by a Basque Government grant IT1628-22, MICIU/AEI/10.13039/501100011033 grants PID2022-136224NB-C21, PID2021-123703NB-C21, PID2022-136510NBC33, PID2024-156016NB-I00, and CEX2024-001451-M, and by USA-NSF grants PHY-2210533 and PHY-2209579. It has also received support from the Horizon Europe research and innovation programme under the Marie Sklodowska-Curie Staff Exchange grant agreement No 101086085 – ASYMMETRY. This project has also been supported by the European Research Council (ERC) under Grant Agreements No. 101039048-GanESS and ERC Advanced Grant 101055120 (ESSCEvNS). This project is also supported by the National Natural Science Foundation of China (12425506, 12375101, 12090060, and 12090064) and the SJTU Double First Class start-up fund (WF220442604). Part of this work used the Solaris cluster, acquired through the Basque Government IT1628-22 grant.

[1] D.Z. Freedman, *Coherent Neutrino Nucleus Scattering as a Probe of the Weak Neutral Current*, *Phys. Rev. D* **9** (1974) 1389.

[2] COHERENT collaboration, *Observation of Coherent Elastic Neutrino-Nucleus Scattering*, *Science* **357** (2017) 1123 [1708.01294].

[3] B. Scholz, *First Observation of Coherent Elastic Neutrino-Nucleus Scattering*, Ph.D. thesis, 2018. 1904.01155. https://doi.org/10.1007/978-3-319-99747-6.

[4] F.T. Avignone and Y.V. Efremenko, *Neutrino nucleus cross-section measurements at intense, pulsed spallation sources*, *J. Phys. G* **29** (2003) 2615.

[5] Y. Efremenko and W.R. Hix, *Opportunities for Neutrino Physics at the Spallation Neutron Source (SNS)*, *J. Phys. Conf. Ser.* **173** (2009) 012006 [0807.2801].

[6] J.I. Collar et al., *Coherent neutrino-nucleus scattering detection with a CsI[Na] scintillator at the SNS spallation source*, *Nucl. Instrum. Meth. A* **773** (2015) 56 [1407.7524].

[7] N.E. Fields, Ph.D. thesis, University of Chicago, 2014.

[8] G.T. Natti, É.R.T. Natti and P.L. Natti, *Industrial Applications of Neutrinos*, *Braz. J. Phys.* **54** (2024) 241 [2503.11686].

[9] A. Drukier and L. Stodolsky, *Principles and Applications of a Neutral Current Detector for Neutrino Physics and Astronomy*, *Phys. Rev. D* **30** (1984) 2295.

[10] J. Colaresi, J.I. Collar, T.W. Hossbach, C.M. Lewis and K.M. Yocum, *Measurement of Coherent Elastic Neutrino-Nucleus Scattering from Reactor Antineutrinos*, *Phys. Rev. Lett.* **129** (2022) 211802 [2202.09672].

[11] N. Ackermann et al., *Direct observation of coherent elastic antineutrino–nucleus scattering*, *Nature* **643** (2025) 1229 [2501.05206].

[12] Y. Li, G. Herrera and P. Huber, *New Physics versus Quenching Factors in Coherent Neutrino Scattering*, 2502.12308.

[13] XENON collaboration, *First Indication of Solar B8 Neutrinos via Coherent Elastic Neutrino-Nucleus Scattering with XENONnT*, *Phys. Rev. Lett.* **133** (2024) 191002 [2408.02877].

[14] PandaX collaboration, *First Indication of Solar B8 Neutrinos through Coherent Elastic Neutrino-Nucleus Scattering in PandaX-4T*, *Phys. Rev. Lett.* **133** (2024) 191001 [2407.10892].

[15] LZ collaboration, *Searches for Light Dark Matter and Evidence of Coherent Elastic Neutrino-Nucleus Scattering of Solar Neutrinos with the LUX-ZEPLIN (LZ) Experiment*, 2512.08065.

[16] V. De Romeri, D.K. Papoulias and C.A. Ternes, *Bounds on new neutrino interactions from the first CEνNS data at direct detection experiments*, *JCAP* **05** (2025) 012 [2411.11749].

[17] D. Aristizabal Sierra, N. Mishra and L. Strigari, *Implications of first neutrino-induced nuclear recoil measurements in direct detection experiments: Probing nonstandard interaction via CEνNS*, *Phys. Rev. D* **111** (2025) 055007 [2409.02003].

[18] D. Baxter et al., *Coherent Elastic Neutrino-Nucleus Scattering at the European Spallation Source*, *JHEP* **02** (2020) 123 [1911.00762].

[19] ESSnuSB collaboration, *The ESSnuSB Design Study: Overview and Future Prospects*, *Universe* **9** (2023) 347 [2303.17356].

[20] https://j-parc.jp/c/en/press-release/2024/05/31001348.html.

[21] H. Abele et al., *Particle Physics at the European Spallation Source*, *Phys. Rept.* **1023** (2023) 1 [2211.10396].

[22] K.J. Kelly, P.A.N. Machado, A. Marchionni and Y.F. Perez-Gonzalez, *LEvEL: Low-Energy Neutrino Experiment at the LHC*, *JHEP* **08** (2021) 087 [2103.00009].

[23] K.Scholberg, *Coherent Elastic Neutrino-Nucleus Scattering*, 2019. Talk at *16th International Conference on Topcs in Astroparticle Physics (TAUP2019)*, Toyama, September 2019, https://www-kam2.icrr.u-tokyo.ac.jp/event/3/contributions/241/attachments/168/192/Web_PLENARY_SESSIONS_Fri1_Scholberg.pdf.

[24] JSNS2 collaboration, *Technical Design Report (TDR): Searching for a Sterile Neutrino at J-PARC MLF (E56, JSNS2)*, 1705.08629.

[25] V. Bresó-Pla, S. Cruz-Alzaga, M. González-Alonso and S. Prakash, *Muon-Decay Parameters from COHERENT*, *Phys. Rev. Lett.* **135** (2025) 131802 [2502.18175].

[26] JSNS2 collaboration, *Proposal: A Search for Sterile Neutrino at J-PARC Materials and Life Science Experimental Facility*, 1310.1437.

[27] COHERENT collaboration, *A D_2O detector for flux normalization of a pion decay-at-rest neutrino source*, *JINST* **16** (2021) P08048 [2104.09605].

[28] D. Pelowitz *et al.*, 2011 MCNPX User's Manual Version 2.7.0 LA-CP-11-00438.

[29] JSNS2 collaboration, *The first JSNS^2 measurement of electron neutrino flux using $^{12}C(\nu_e, e^-)^{12}N_{g.s.}$ reaction*, 2412.18509.

[30] GEANT4 collaboration, *GEANT4 - A Simulation Toolkit*, *Nucl. Instrum. Meth. A* **506** (2003) 250.

[31] M.S. Gordon, P. Goldhagen, K.P. Rodbell, T.H. Zabel, H.H.K. Tang, J.M. Clem et al., *Measurement of the flux and energy spectrum of cosmic-ray induced neutrons on the ground*, *IEEE Trans. Nucl. Sci.* **51** (2004) 3427.

[32] Z. Hu, L. Ge, J. Sun, Y. Zhang, Z. Cui, G. Gorini et al., *Measurements of cosmic ray induced background neutrons near the ground using a bonner sphere spectrometer*, *Nuclear Instruments and Methods in Physics Research Section A: Accelerators, Spectrometers, Detectors and Associated Equipment* **940** (2019) 78.

[33] T. Sato, *Analytical Model for Estimating the Zenith Angle Dependence of Terrestrial Cosmic Ray Fluxes*, *PLoS One* **11** (2016) e0160390.

[34] A.S. Malgin, *Characteristics of neutrons produced by muons in a standard rock*, *Phys. Atom. Nucl.* **78** (2015) 835.

[35] H.M. Kluck, *Measurement of the Cosmic-Induced Neutron Yield at the Modane Underground Laboratory*, Ph.D. thesis, KIT, Karlsruhe, 2013. 10.1007/978-3-319-18527-9.

[36] C.M. Lewis, *Particle physics in the sub-keV energy regime*, Ph.D. thesis, U. Chicago, 2023. 2310.01314. 10.6082/uchicago.5730.

[37] Presentation by D. Lee at https://indico.phy.ornl.gov/event/217/contributions/.

[38] S. Ajimura et al., *On-site background measurements for the J-PARC E56 experiment: A search for the sterile neutrino at J-PARC MLF*, *Progress of Theoretical and Experimental Physics* **2015** (2015) 63C01.

[39] S. Gardiner, *Simulating low-energy neutrino interactions with MARLEY*, *Comput. Phys. Commun.* **269** (2021) 108123 [2101.11867].

[40] R. Lazauskas and C. Volpe, *Low energy neutrino scattering measurements at future Spallation Source facilities*, *J. Phys. G* **37** (2010) 125101 [1004.0310]. [Erratum: J.Phys.G 42, 059501 (2015)].

[41] COHERENT collaboration, *Measurement of Pbnat(νe,Xn) production with a stopped-pion neutrino source*, *Phys. Rev. D* **108** (2023) 072001 [2212.11295].

[42] G. Matteucci, *Cryogenic sipms for the optical readout of darkside-20k*, *Journal of Instrumentation* **20** (2025) C06010.

[43] P.S. Barbeau et al.*Phys. Rev. D* **109** (2024) 092005 [2311.13032].

[44] C. Su, Q. Liu and T. Liang*Phys. Sci. Forum* **8** (2023) 19 [2303.13423].

[45] C.M. Lewis and J.I. Collar, *Response of undoped cryogenic CsI to low-energy nuclear recoils*, *Phys. Rev. C* **104** (2021) 014612 [2101.03264].

[46] J.I. Collar, C.M. Lewis, A. Simón and S.G. Yoon, *Scintillation response of cryogenic CsI to few-keV and sub-keV nuclear recoils*, 2512.09820.

[47] M. McClish, R. Farrell, F. Olschner, M. Squillante, G. Entine and K. Shah, *Characterization of very large silicon avalanche photodiodes*, in *IEEE Symposium Conference Record Nuclear Science 2004.*, vol. 2, pp. 1270–1273 Vol. 2, 2004, DOI.

[48] L. Baudis, G. Benato, R. Dressler, F. Piastra, I. Usoltsev and M. Walter, *Enhancement of Light Yield and Stability of Radio-Pure Tetraphenyl-Butadiene Based Coatings for VUV Light Detection in Cryogenic Environments*, *JINST* **10** (2015) P09009 [1503.05349].

[49] G.R. Araujo, T. Pollmann and A. Ulrich, *Photoluminescence response of acrylic (PMMA) and polytetrafluoroethylene (PTFE) to ultraviolet light*, *Eur. Phys. J. C* **79** (2019) 653 [1905.03044].

[50] DarkSide-20k collaboration, *Production of the DarkSide-20k photo-detectors*, *Nucl. Instrum. Meth. A* **1068** (2024) 169723.

[51] Shanghai Institute of Ceramics, Chinese Academy of Sciences (SICCAS), 1295 Dingxi Road, Shanghai 200050, China.

[52] J.I. Collar, A.R.L. Kavner and C.M. Lewis*Phys. Rev. D* **103** (2021) 122003 [arXiv:2102.10089].

[53] P.S. Barbeau, J.I. Collar and O. Tench, *Large-Mass Ultra-Low Noise Germanium Detectors: Performance and Applications in Neutrino and Astroparticle Physics*, *JCAP* **09** (2007) 009 [https://arxiv.org/abs/nucl-ex/0701012].

[54] J. Colaresi, J.I. Collar, T.W. Hossbach, A.R.L. Kavner, C.M. Lewis, A.E. Robinson et al., *First results from a search for coherent elastic neutrino-nucleus scattering at a reactor site*, *Phys. Rev. D* **104** (2021) 072003 [2108.02880].

[55] NEXT collaboration, *The NEXT-100 Detector*, 2505.17848.

[56] NEXT collaboration, *The Next White (NEW) Detector*, *JINST* **13** (2018) P12010 [1804.02409].

[57] NEXT collaboration, *Radiogenic Backgrounds in the NEXT Double Beta Decay Experiment*, *JHEP* **10** (2019) 051 [1905.13625].

[58] B.C. Cañas, E.A. Garcés, O.G. Miranda and A. Parada, *Future perspectives for a weak mixing angle measurement in coherent elastic neutrino nucleus scattering experiments*, *Phys. Lett. B* **784** (2018) 159 [1806.01310].

[59] M. Cadeddu and F. Dordei, *Reinterpreting the weak mixing angle from atomic parity violation in view of the Cs neutron rms radius measurement from COHERENT*, *Phys. Rev. D* **99** (2019) 033010 [1808.10202].

[60] X.-R. Huang and L.-W. Chen, *Neutron Skin in CsI and Low-Energy Effective Weak Mixing Angle from COHERENT Data*, *Phys. Rev. D* **100** (2019) 071301 [1902.07625].

[61] M. Cadeddu, F. Dordei, C. Giunti, Y.F. Li and Y.Y. Zhang, *Neutrino, electroweak, and nuclear physics from COHERENT elastic neutrino-nucleus scattering with refined quenching factor*, Phys. Rev. D **101** (2020) 033004 [1908.06045].

[62] M. Cadeddu, F. Dordei, C. Giunti, Y.F. Li, E. Picciau and Y.Y. Zhang, *Physics results from the first COHERENT observation of coherent elastic neutrino-nucleus scattering in argon and their combination with cesium-iodide data*, Phys. Rev. D **102** (2020) 015030 [2005.01645].

[63] M. Cadeddu et al., *New insights into nuclear physics and weak mixing angle using electroweak probes*, Phys. Rev. C **104** (2021) 065502 [2102.06153].

[64] M. Atzori Corona, M. Cadeddu, N. Cargioli, F. Dordei, C. Giunti and G. Masia, *Nuclear neutron radius and weak mixing angle measurements from latest COHERENT CsI and atomic parity violation Cs data*, Eur. Phys. J. C **83** (2023) 683 [2303.09360].

[65] M. Atzori Corona, M. Cadeddu, N. Cargioli, G. Co', F. Dordei and C. Giunti, *Joint analysis of reactor and accelerator CEnNS data on germanium: implications for the Standard Model and nuclear physics*, 2506.13555.

[66] M. Cadeddu, C. Giunti, Y.F. Li and Y.Y. Zhang, *Average CsI neutron density distribution from COHERENT data*, Phys. Rev. Lett. **120** (2018) 072501 [1710.02730].

[67] E. Ciuffoli, J. Evslin, Q. Fu and J. Tang, *Extracting nuclear form factors with coherent neutrino scattering*, Phys. Rev. D **97** (2018) 113003 [1801.02166].

[68] D.K. Papoulias, T.S. Kosmas, R. Sahu, V.K.B. Kota and M. Hota, *Constraining nuclear physics parameters with current and future COHERENT data*, Phys. Lett. B **800** (2020) 135133 [1903.03722].

[69] P. Coloma, I. Esteban, M.C. Gonzalez-Garcia and J. Menendez, *Determining the nuclear neutron distribution from Coherent Elastic neutrino-Nucleus Scattering: current results and future prospects*, JHEP **08** (2020) 030 [2006.08624].

[70] J. Barranco, O.G. Miranda and T.I. Rashba, *Probing new physics with coherent neutrino scattering off nuclei*, JHEP **12** (2005) 021 [hep-ph/0508299].

[71] J.A. Formaggio, E. Figueroa-Feliciano and A.J. Anderson, *Sterile neutrinos, coherent scattering and oscillometry measurements with low-temperature bolometers*, Phys. Rev. D **85** (2012) 013009 [1107.3512].

[72] A.J. Anderson et al., *Measuring active-to-sterile neutrino oscillations with neutral current coherent neutrino-nucleus scattering*, Phys. Rev. D **86** (2012) 013004 [1201.3805].

[73] B. Dutta, Y. Gao, R. Mahapatra, N. Mirabolfathi, L.E. Strigari and J.W. Walker, *Sensitivity to oscillation with a sterile fourth generation neutrino from ultra-low threshold neutrino-nucleus coherent scattering*, Phys. Rev. D **94** (2016) 093002 [1511.02834].

[74] D.G. Cerdeño, M. Fairbairn, T. Jubb, P.A.N. Machado, A.C. Vincent and C. Bœhm, *Physics from solar neutrinos in dark matter direct detection experiments*, JHEP **05** (2016) 118 [1604.01025]. [Erratum: JHEP 09, 048 (2016)].

[75] J.B. Dent, B. Dutta, S. Liao, J.L. Newstead, L.E. Strigari and J.W. Walker, *Probing light mediators at ultralow threshold energies with coherent elastic neutrino-nucleus scattering*, Phys. Rev. D **96** (2017) 095007 [1612.06350].

[76] P. Coloma, P.B. Denton, M.C. Gonzalez-Garcia, M. Maltoni and T. Schwetz, *Curtailing the dark side in non-standard neutrino interactions*, JHEP **04** (2017) 116 [1701.04828].

[77] T.S. Kosmas, D.K. Papoulias, M. Tórtola and J.W.F. Valle, *Probing light sterile neutrino signatures at reactor and spallation neutron source neutrino experiments*, Phys. Rev. D **96** (2017) 063013 [1703.00054].

[78] S.-F. Ge and I.M. Shoemaker, *Constraining photon portal dark matter with TEXONO and COHERENT data*, JHEP **11** (2018) 066 [1710.10889].

[79] I.M. Shoemaker, *COHERENT search strategy for beyond standard model neutrino interactions*, Phys. Rev. D **95** (2017) 115028 [1703.05774].

[80] P. Coloma, M.C. Gonzalez-Garcia, M. Maltoni and T. Schwetz, *COHERENT enlightenment of the neutrino dark side*, Phys. Rev. D **96** (2017) 115007 [1708.02899].

[81] J. Liao and D. Marfatia, *COHERENT constraints on nonstandard neutrino interactions*, Phys. Lett. B **775** (2017) 54 [1708.04255].

[82] B.C. Cañas, E.A. Garcés, O.G. Miranda and A. Parada, *The reactor antineutrino anomaly and low energy threshold neutrino experiments*, Phys. Lett. B **776** (2018) 451 [1708.09518].

[83] J.B. Dent, B. Dutta, S. Liao, J.L. Newstead, L.E. Strigari and J.W. Walker, *Accelerator and reactor complementarity in coherent neutrino-nucleus scattering*, Phys. Rev. D **97** (2018) 035009 [1711.03521].

[84] D.K. Papoulias and T.S. Kosmas, *COHERENT constraints to conventional and exotic neutrino physics*, Phys. Rev. D **97** (2018) 033003 [1711.09773].

[85] Y. Farzan, M. Lindner, W. Rodejohann and X.-J. Xu, *Probing neutrino coupling to a light scalar with coherent neutrino scattering*, JHEP **05** (2018) 066 [1802.05171].

[86] J. Billard, J. Johnston and B.J. Kavanagh, *Prospects for exploring new physics in coherent elastic neutrino-nucleus scattering*, JCAP **11** (2018) 016 [1805.01798].

[87] P. Coloma, I. Esteban, M.C. Gonzalez-Garcia and M. Maltoni, *Improved global fit to non-standard neutrino interactions using COHERENT energy and timing data*, JHEP **02** (2020) 023 [1911.09109]. [Addendum: JHEP 12, 071 (2020)].

[88] M. Chaves and T. Schwetz, *Resolving the LMA-dark NSI degeneracy with coherent neutrino-nucleus scattering*, JHEP **05** (2021) 042 [2102.11981].

[89] D. Aristizabal Sierra, V. De Romeri and N. Rojas, *COHERENT analysis of neutrino generalized interactions*, Phys. Rev. D **98** (2018) 075018 [1806.07424].

[90] V. Brdar, W. Rodejohann and X.-J. Xu, *Producing a new fermion in coherent elastic neutrino-nucleus scattering: from neutrino mass to dark matter*, JHEP **12** (2018) 024 [1810.03626].

[91] M. Cadeddu, C. Giunti, K.A. Kouzakov, Y.-F. Li, Y.-Y. Zhang and A.I. Studenikin, *Neutrino Charge Radii From Coherent Elastic Neutrino-nucleus Scattering*, *Phys. Rev. D* **98** (2018) 113010 [1810.05606]. [Erratum: Phys.Rev.D 101, 059902 (2020)].

[92] C. Blanco, D. Hooper and P. Machado, *Constraining sterile neutrino interpretations of the LSND and MiniBooNE anomalies with coherent neutrino scattering experiments*, *Phys. Rev. D* **101** (2020) 075051 [1901.08094].

[93] B. Dutta, S. Liao, S. Sinha and L.E. Strigari, *Searching for beyond the Standard Model physics with COHERENT energy and timing data*, *Phys. Rev. Lett.* **123** (2019) 061801 [1903.10666].

[94] O.G. Miranda, D.K. Papoulias, M. Tórtola and J.W.F. Valle, *Probing neutrino transition magnetic moments with coherent elastic neutrino-nucleus scattering*, *JHEP* **07** (2019) 103 [1905.03750].

[95] CONNIE collaboration, *Exploring low-energy neutrino physics with the Coherent Neutrino Nucleus Interaction Experiment*, *Phys. Rev. D* **100** (2019) 092005 [1906.02200].

[96] B. Dutta, D. Kim, S. Liao, J.-C. Park, S. Shin and L.E. Strigari, *Dark matter signals from timing spectra at neutrino experiments*, *Phys. Rev. Lett.* **124** (2020) 121802 [1906.10745].

[97] D.K. Papoulias, *COHERENT constraints after the COHERENT-2020 quenching factor measurement*, *Phys. Rev. D* **102** (2020) 113004 [1907.11644].

[98] A.N. Khan and W. Rodejohann, *New physics from COHERENT data with an improved quenching factor*, *Phys. Rev. D* **100** (2019) 113003 [1907.12444].

[99] C. Giunti, *General COHERENT constraints on neutrino nonstandard interactions*, *Phys. Rev. D* **101** (2020) 035039 [1909.00466].

[100] B.C. Cañas, E.A. Garcés, O.G. Miranda, A. Parada and G. Sánchez García, *Interplay between nonstandard and nuclear constraints in coherent elastic neutrino-nucleus scattering experiments*, *Phys. Rev. D* **101** (2020) 035012 [1911.09831].

[101] O.G. Miranda, D.K. Papoulias, M. Tórtola and J.W.F. Valle, *Probing new neutral gauge bosons with CEνNS and neutrino-electron scattering*, *Phys. Rev. D* **101** (2020) 073005 [2002.01482].

[102] L.J. Flores, N. Nath and E. Peinado, *Non-standard neutrino interactions in U(1)' model after COHERENT data*, *JHEP* **06** (2020) 045 [2002.12342].

[103] O.G. Miranda, D.K. Papoulias, G. Sanchez Garcia, O. Sanders, M. Tórtola and J.W.F. Valle, *Implications of the first detection of coherent elastic neutrino-nucleus scattering (CEvNS) with Liquid Argon*, *JHEP* **05** (2020) 130 [2003.12050]. [Erratum: JHEP 01, 067 (2021)].

[104] N. Hurtado, H. Mir, I.M. Shoemaker, E. Welch and J. Wyenberg, *Dark matter-neutrino interconversion at COHERENT, direct detection, and the early Universe*, *Phys. Rev. D* **102** (2020) 015006 [2005.13384].

[105] O.G. Miranda, D.K. Papoulias, O. Sanders, M. Tórtola and J.W.F. Valle, *Future CEνNS experiments as probes of lepton unitarity and light-sterile neutrinos*, *Phys. Rev. D* **102** (2020) 113014 [2008.02759].

[106] M. Cadeddu et al., *Constraints on light vector mediators through coherent elastic neutrino nucleus scattering data from COHERENT*, *JHEP* **01** (2021) 116 [2008.05022].

[107] I.M. Shoemaker and E. Welch, *Sailing the CEνNS seas of non-standard neutrino interactions with the coherent CAPTAIN Mills experiment*, 2103.08401.

[108] L.M.G. de la Vega, L.J. Flores, N. Nath and E. Peinado, *Complementarity between dark matter direct searches and CEνNS experiments in U(1)' models*, *JHEP* **09** (2021) 146 [2107.04037].

[109] J. Liao, H. Liu and D. Marfatia, *Coherent neutrino scattering and the Migdal effect on the quenching factor*, *Phys. Rev. D* **104** (2021) 015005 [2104.01811].

[110] CONUS collaboration, *Novel constraints on neutrino physics beyond the standard model from the CONUS experiment*, 2110.02174.

[111] L.J. Flores, N. Nath and E. Peinado, *CEνNS as a probe of flavored generalized neutrino interactions*, *Phys. Rev. D* **105** (2022) 055010 [2112.05103].

[112] Y.-F. Li and S.-y. Xia, *Constraining light mediators via detection of coherent elastic solar neutrino nucleus scattering*, *Nucl. Phys. B* **977** (2022) 115737 [2201.05015].

[113] D. Aristizabal Sierra, J. Liao and D. Marfatia, *Impact of form factor uncertainties on interpretations of coherent elastic neutrino-nucleus scattering data*, *JHEP* **06** (2019) 141 [1902.07398].

[114] M. Abdullah, D. Aristizabal Sierra, B. Dutta and L.E. Strigari, *Coherent elastic neutrino-nucleus scattering with directional detectors*, *Phys. Rev. D* **102** (2020) 015009 [2003.11510].

[115] G. Fernandez-Moroni et al., *The physics potential of a reactor neutrino experiment with Skipper-CCDs: searching for new physics with light mediators*, *JHEP* **02** (2022) 127 [2108.07310].

[116] E. Bertuzzo, G.G. di Cortona and L.M.D. Ramos, *Probing light vector mediators with coherent scattering at future facilities*, 2112.04020.

[117] CONUS collaboration, *First upper limits on neutrino electromagnetic properties from the CONUS experiment*, *Eur. Phys. J. C* **82** (2022) 813 [2201.12257].

[118] V. De Romeri, O.G. Miranda, D.K. Papoulias, G. Sanchez Garcia, M. Tórtola and J.W.F. Valle, *Physics implications of a combined analysis of COHERENT CsI and LAr data*, *JHEP* **04** (2023) 035 [2211.11905].

[119] P. Coloma, I. Esteban, M.C. Gonzalez-Garcia, L. Larizgoitia, F. Monrabal and S. Palomares-Ruiz, *Bounds on new physics with data of the Dresden-II reactor experiment and COHERENT*, *JHEP* **05** (2022) 037 [2202.10829].

[120] *J-PARC Annual Report*, 2020. https://j-parc.jp/documents/annual_report/J_PARC_AR2020.pdf.

[121] *J-PARC Annual Report*, 2021. https://www.j-parc.jp/c/uploads/2023/J_PARC_AR2021_s.pdf.

[122] *J-PARC Annual Report*, 2022. https://j-parc.jp/c/uploads/2024/J_PARC_AnnualReport2022_s.pdf.

[123] J. Erler and R. Ferro-Hernández, *Weak Mixing Angle in the Thomson Limit*, *JHEP* **03** (2018) 196 [1712.09146].

[124] C. Giunti and A. Studenikin, *Neutrino electromagnetic interactions: a window to new physics*, *Rev. Mod. Phys.* **87** (2015) 531 [1403.6344].

[125] G. Degrassi, A. Sirlin and W.J. Marciano, *Effective Electromagnetic Form-factor of the Neutrino*, *Phys. Rev. D* **39** (1989) 287.

[126] P. Vogel and J. Engel, *Neutrino electromagnetic form-factors*, *Phys. Rev. D* **39** (1989) 3378.

[127] K.A. Kouzakov and A.I. Studenikin, *Electromagnetic properties of massive neutrinos in low-energy elastic neutrino-electron scattering*, *Phys. Rev. D* **95** (2017) 055013 [1703.00401]. [Erratum: Phys.Rev.D 96, 099904 (2017)].

[128] J. Bernabeu, L.G. Cabral-Rosetti, J. Papavassiliou and J. Vidal, *On the charge radius of the neutrino*, *Phys. Rev. D* **62** (2000) 113012 [hep-ph/0008114].

[129] J. Bernabeu, J. Papavassiliou and J. Vidal, *On the observability of the neutrino charge radius*, *Phys. Rev. Lett.* **89** (2002) 101802 [hep-ph/0206015]. [Erratum: Phys.Rev.Lett. 89, 229902 (2002)].

[130] J. Bernabeu, J. Papavassiliou and J. Vidal, *The Neutrino charge radius is a physical observable*, *Nucl. Phys. B* **680** (2004) 450 [hep-ph/0210055].

[131] R.H. Helm, *Inelastic and Elastic Scattering of 187-Mev Electrons from Selected Even-Even Nuclei*, *Phys. Rev.* **104** (1956) 1466.

[132] I. Angeli and K. Marinova, *Table of experimental nuclear ground state charge radii: An update*, *Atom. Data Nucl. Data Tabl.* **99** (2013) 69.

[133] Particle Data Group collaboration, *Review of particle physics*, *Phys. Rev. D* **110** (2024) 030001.

[134] A. Trzcinska, J. Jastrzebski, P. Lubinski, F. Hartmann, R. Schmidt, T. von Egidy et al., *Neutron density distributions deduced from anti-protonic atoms*, *Phys. Rev. Lett.* **87** (2001) 082501.

[135] J.R. de Laeter, J.K. Böhlke, P.D. Bièvre, H. Hidaka, H.S. Peiser, K.J.R. Rosman et al., *Atomic weights of the elements. Review 2000 (IUPAC Technical Report)*, *Pure and Applied Chemistry* **75** (2003) 683 .

[136] J.I. Collar, A.R.L. Kavner and C.M. Lewis, *Response of CsI[Na] to nuclear recoils: Impact on coherent elastic neutrino-nucleus scattering*, *Phys. Rev. D* **100** (2019) 033003 [https://arxiv.org/abs/1907.04828].

[137] SLAC E158 collaboration, *Precision measurement of the weak mixing angle in Moller scattering*, *Phys. Rev. Lett.* **95** (2005) 081601 [hep-ex/0504049].

[138] Qweak collaboration, *Precision measurement of the weak charge of the proton*, *Nature* **557** (2018) 207 [1905.08283].

[139] C.S. Wood, S.C. Bennett, D. Cho, B.P. Masterson, J.L. Roberts, C.E. Tanner et al., *Measurement of parity nonconservation and an anapole moment in cesium*, *Science* **275** (1997) 1759.

[140] V.A. Dzuba, J.C. Berengut, V.V. Flambaum and B. Roberts, *Revisiting parity non-conservation in cesium*, *Phys. Rev. Lett.* **109** (2012) 203003 [1207.5864].

[141] COHERENT collaboration, *Measurement of the Coherent Elastic Neutrino-Nucleus Scattering Cross Section on CsI by COHERENT*, *Phys. Rev. Lett.* **129** (2022) 081801 [2110.07730].

[142] C. Giunti, K. Kouzakov, Y.-F. Li and A. Studenikin, *Neutrino Electromagnetic Properties*, 2411.03122.

[143] M. Atzori Corona, M. Cadeddu, N. Cargioli, F. Dordei, C. Giunti, Y.F. Li et al., *Impact of the Dresden-II and COHERENT neutrino scattering data on neutrino electromagnetic properties and electroweak physics*, *JHEP* **09** (2022) 164 [2205.09484].

[144] M. Atzori Corona, M. Cadeddu, N. Cargioli, F. Dordei and C. Giunti, *Momentum dependent flavor radiative corrections to the coherent elastic neutrino-nucleus scattering for the neutrino charge-radius determination*, *JHEP* **05** (2024) 271 [2402.16709].

[145] COHERENT collaboration, *First Measurement of Coherent Elastic Neutrino-Nucleus Scattering on Argon*, *Phys. Rev. Lett.* **126** (2021) 012002 [2003.10630].

[146] C. Horowitz et al., *Weak charge form factor and radius of 208Pb through parity violation in electron scattering*, *Phys. Rev. C* **85** (2012) 032501 [1202.1468].

[147] T. Donnelly and I. Sick, *ELASTIC MAGNETIC ELECTRON SCATTERING FROM NUCLEI*, *Rev. Mod. Phys.* **56** (1984) 461.

[148] S. Abrahamyan et al., *Measurement of the Neutron Radius of 208Pb Through Parity-Violation in Electron Scattering*, *Phys. Rev. Lett.* **108** (2012) 112502 [1201.2568].

[149] PREX collaboration, *Accurate Determination of the Neutron Skin Thickness of ^{208}Pb through Parity-Violation in Electron Scattering*, *Phys. Rev. Lett.* **126** (2021) 172502 [2102.10767].

[150] C. Garcia-Recio, J. Nieves and E. Oset, *Neutron distributions from pionic atoms*, *Nucl. Phys. A* **547** (1992) 473.

[151] T. Suzuki et al., *Neutron skin of Na isotopes studied via the interaction cross-sections*, *Phys. Rev. Lett.* **75** (1995) 3241.

[152] B. Clark, L. Kerr and S. Hama, *Neutron densities from a global analysis of medium-energy proton nucleus elastic scattering*, *Phys. Rev. C* **67** (2003) 054605 [nucl-th/0209052].

[153] V. Lapoux, V. Somà, C. Barbieri, H. Hergert, J. Holt and S. Stroberg, *Radii and Binding Energies in Oxygen Isotopes: A Challenge for Nuclear Forces*, *Phys. Rev. Lett.* **117** (2016) 052501 [1605.07885].

[154] C. Tarbert et al., *Neutron skin of ^{208}Pb from Coherent Pion Photoproduction*, *Phys. Rev. Lett.* **112** (2014) 242502 [1311.0168].

[155] G. Co', M. Anguiano and A. Lallena, *Nuclear structure uncertainties in coherent elastic neutrino-nucleus scattering*, *JCAP* **04** (2020) 044 [2001.04684].

[156] M. Hoferichter, P. Klos, J. Menéndez and A. Schwenk, *Nuclear structure factors for general spin-independent WIMP-nucleus scattering*, *Phys. Rev.* **D99** (2019) 055031 [1812.05617].

[157] M. Hoferichter, J. Menéndez and A. Schwenk, *Coherent elastic neutrino-nucleus scattering: EFT analysis and nuclear responses*, *Phys. Rev. D* **102** (2020) 074018 [2007.08529].

[158] P. Coloma, M.C. Gonzalez-Garcia, M. Maltoni, J.P. Pinheiro and S. Urrea, *Global constraints on non-standard neutrino interactions with quarks and electrons*, *JHEP* **08** (2023) 032 [2305.07698].

[159] O.G. Miranda, M.A. Tortola and J.W.F. Valle, *Are solar neutrino oscillations robust?*, *JHEP* **10** (2006) 008 [hep-ph/0406280].

[160] M.C. Gonzalez-Garcia and M. Maltoni, *Determination of matter potential from global analysis of neutrino oscillation data*, *JHEP* **09** (2013) 152 [1307.3092].

[161] P. Coloma and T. Schwetz, *Generalized mass ordering degeneracy in neutrino oscillation experiments*, *Phys.*

Rev. **D94** (2016) 055005 [1604.05772]. [Erratum: Phys. Rev.D95,no.7,079903(2017)].

[162] I. Esteban, M.C. Gonzalez-Garcia, M. Maltoni, I. Martinez-Soler and J. Salvado, *Updated constraints on non-standard interactions from global analysis of oscillation data*, *JHEP* **08** (2018) 180 [1805.04530]. [Addendum: JHEP 12, 152 (2020)].

[163] K. Scholberg, *Prospects for measuring coherent neutrino-nucleus elastic scattering at a stopped-pion neutrino source*, *Phys. Rev. D* **73** (2006) 033005 [hep-ex/0511042].

[164] P. Langacker, *The Physics of Heavy Z' Gauge Bosons*, *Rev. Mod. Phys.* **81** (2009) 1199 [0801.1345].

[165] M. Fabbrichesi, E. Gabrielli and G. Lanfranchi, *The Dark Photon*, 2005.01515.

[166] M. Cirelli, E. Del Nobile and P. Panci, *Tools for model-independent bounds in direct dark matter searches*, *JCAP* **10** (2013) 019 [1307.5955].

[167] M. Atzori Corona, M. Cadeddu, N. Cargioli, F. Dordei, C. Giunti, Y.F. Li et al., *Probing light mediators and g-2 through detection of coherent elastic neutrino nucleus scattering at COHERENT*, *JHEP* **05** (2022) 109 [2202.11002].

[168] J. Liao, H. Liu and D. Marfatia, *Implications of the first evidence for coherent elastic scattering of reactor neutrinos*, *Phys. Rev. D* **106** (2022) L031702 [2202.10622].

[169] Borexino collaboration, *Limiting neutrino magnetic moments with Borexino Phase-II solar neutrino data*, *Phys. Rev. D* **96** (2017) 091103 [1707.09355].

[170] P. Coloma, M.C. Gonzalez-Garcia, M. Maltoni, J.P. Pinheiro and S. Urrea, *Constraining new physics with Borexino Phase-II spectral data*, *JHEP* **07** (2022) 138 [2204.03011]. [Erratum: JHEP 11, 138 (2022)].

[171] V.V. Barinov et al., *Results from the Baksan Experiment on Sterile Transitions (BEST)*, *Phys. Rev. Lett.* **128** (2022) 232501 [2109.11482].

[172] NOvA collaboration, *Dual-Baseline Search for Active-to-Sterile Neutrino Oscillations in NOvA*, *Phys. Rev. Lett.* **134** (2025) 081804 [2409.04553].

[173] MINOS+, Daya Bay collaboration, *Improved Constraints on Sterile Neutrino Mixing from Disappearance Searches in the MINOS, MINOS+, Daya Bay, and Bugey-3 Experiments*, *Phys. Rev. Lett.* **125** (2020) 071801 [2002.00301].

[174] SciBooNE, MiniBooNE collaboration, *Dual baseline search for muon neutrino disappearance at* $0.5\mathrm{eV}^2 < \Delta m^2 < 40\mathrm{eV}^2$, *Phys. Rev. D* **85** (2012) 032007 [1106.5685].

[175] I.E. Stockdale et al., *Limits on Muon Neutrino Oscillations in the Mass Range 55-eV**2 < Delta m**2 < 800-eV**2*, *Phys. Rev. Lett.* **52** (1984) 1384.

[176] I.A. Bisset, B. Dutta, W.-C. Huang and L.E. Strigari, *Short baseline neutrino anomalies at stopped pion experiments*, *JHEP* **10** (2024) 003 [2310.13194].

[177] M.A. Acero, C. Giunti and M. Laveder, *Limits on nu(e) and anti-nu(e) disappearance from Gallium and reactor experiments*, *Phys. Rev. D* **78** (2008) 073009 [0711.4222].

[178] M.C. Gonzalez-Garcia, M. Maltoni and J.P. Pinheiro, *Solar model independent constraints on the sterile neutrino interpretation of the Gallium Anomaly*, *Phys. Lett. B* **862** (2025) 139297 [2411.16840].

[179] KATRIN collaboration, *Sterile-neutrino search based on 259 days of KATRIN data*, 2503.18667.